Faculté des sciences

Quantification of log-based QA uncertainties based on measurements in proton PBS beams

Mémoire présenté en vue de l'obtention du grade académique de
Master [120] en sciences physiques, à finalité spécialisée: physique médicale

Auteur : Thomas Stinglhamber
Promoteur : Pr. Edmond Sterpin
Lecteurs : Pr. Eduardo Cortina, Dr. Séverine Rossomme, Dr. Kevin Souris
École de physique
Année académique 2022-2023

Acknowledgements

I would like to take this opportunity to express my heartfelt gratitude to everyone who has contributed to the completion of this thesis.

First and foremost, I would like to thank Edmond Sterpin, my teacher and promoter, for having trusted me and for having proposed a subject in partnership with IBA (Ion Beam Application) so late in the year.

I extend my sincerest appreciation to IBA, the company that proposed the subject of my thesis. Their unwavering support, and resources were critical to the successful completion of this project.

I am also grateful to my coordinators, Kevin Souris, Séverine Rossomme, and Thomas Reniers, who worked at IBA and participated in my night measurements in Groningen. Their technical guidance, constructive feedback, and constant support were invaluable in helping me navigate the complexities of the research process.

I would also like to acknowledge the contributions of the IBA team at Groningen, particularly Lennert Leijendekker, the technician who provided us with assistance whenever there was a problem. His dedication and expertise were instrumental in ensuring the smooth functioning of the measurements.

Contents

List of Figures

List of Tables

Chapter 1

Introduction

1.1 Motivation of the study

Before a patient can undergo a proton therapy, a treatment plan must be drawn up. This involves determining where and with what dose the patient will be irradiated, based on his or her anatomy and the location of the tumor. This treatment plan is produced using the Treatment Planning System (TPS), which calculates the dose in 3D within the patient's anatomy. One method of delivering the treatment plan is to use a very narrow protons beam known as a "pencil beam". This beam is bent by two magnets to change direction and scan (in X and Y coordinate) the tumor layer by layer (Z coordinate).

To verify the feasibility and accuracy of the machine-generated plan, it must undergo a quality assurance process called Patient-Specific Quality Assurance (PSQA) as small deviations between the intended and the delivered therapy dose distributions can potentially lead to severe clinical consequences. Since each treatment plan is unique for each patient, this process is necessary to ensure compliance.

One of the methods used to check whether the machine is capable of reproducing this treatment is to make direct measurements using a 2D detector, known as measurement-based quality assurance method. Thus, if the dose distribution measured with the detector matches that planned by the TPS, the treatment is validated. However, this method has its drawbacks.

Measurement-based QA methods are time-consuming for physicists, requiring dedicated beam time and extensive manual measurements. This process limits the number of patients that can be treated. In addition, the information obtained by measurement-based QA is limited. When a detector is used, measurements are typically limited to a few 2D layers within the 3D treatment, and they do not directly capture the patient's specific anatomy. Consequently, the comparison of results is restricted to a layer-by-layer analysis with the treatment planning system (TPS).

To address these challenges and enhance patient-specific QA, log-based QA has emerged as a promising alternative. Log are files that store a history of events that have occurred on the machine. Log files generated during proton therapy treatment capture comprehensive information about the delivery process, including beam position or Monitor Unit[1] delivery. This information used together with Monte Carlo computations can be used to assess the actual dose delivered to the patient during the full treatment and perform QA without the need for additional detectors, thereby eliminating the limitations associated with measurement-based QA.

However, log-based QA is not without its challenges. Uncertainties can arise from various sources, such as inaccuracies in position. These uncertainties must be carefully characterized and mitigated to ensure the reliability and accuracy of log-based QA. Developing a comprehensive model of error is crucial to quantifying and understanding the sources of uncertainty, including their parameters and potential impacts on dose reconstruction.

The primary aim of this thesis is to improve the quality assurance of proton treatment through the utilization of log files corrected by measurements acquired with a flat panel detector. This will involve incorporating the uncertainties inherent in the log files by constructing an error model.

1.2 Structure

This thesis is composed of 6 distinct chapters, which together make it possible to apprehend the fundamental concept of modern therapy by ionization beam and its challenges.

Chapter 1 is about the motivation of this study and why research is still needed in this field.

Chapter 2 provides an overview of modern cancer treatment, including the workflow and various steps involved in establishing a treatment plan. The chapter explores the tools available for validate a treatment plan and their potential for improvement. Additionally, the chapter discusses the limitations of certain new techniques and strategies to overcome them in order to develop future treatments.

Chapter 3 delves into the theoretical aspects of proton therapy. It examines the physics of protons and their interactions. In this chapter, essential concepts are introduced for understanding the material used, such as the flat panel detector.

Chapter 4 discusses about all the material that there must have been to carry out our measurements and especially what was the methodology applied to ensure the accuracy of our measurements.

Chapter 5 presents the results of uncertainties obtained after conducting the measurement sessions. It starts by discussing the average errors associated with each parameter for both detector directions (X and Y) and experimental errors. Then, it delves into analyzing the spot-by-spot errors associated with each parameter and interpolating them.

---

[1] Quantity directly related to the dose.

Chapter 6 presents a synthesis of all the results obtained throughout the analysis, as well as some suggestions for improving the accuracy of future measurements.

Chapter 2

State of the art

The objective of this section is to provide an understanding of proton therapy, a cutting-edge approach in radiation therapy for cancer treatment. It will delve into the unique aspects and advantages of proton therapy compared to conventional treatment methods. Moreover, a primary focus on quality assurance (QA) procedures in proton therapy is made, aiming to improve the efficacy of patient-specific QA.

2.1 Cancer treatment today

Our body is made up of more than 100 trillion cells, which are the smallest building blocks of the human body. The body typically has the appropriate number of cells because cells emit signals that control their ability to divide and grow. When these signals are not present, cells could start to grow out of control and develop into tumors [23]. On a global scale, it is anticipated that 9.6 million people died from cancer in 2018, making it the second largest cause of death [14]. The most typical cancers include :

- Lung (2.09 million cases)
- Breast (2.09 million cases)
- Colorectal (1.80 million cases)
- Prostate (1.28 million cases)
- Skin cancer (non-melanoma) (1.04 million cases).

To cure these cancers, there are 3 main classes of care [22] :

- Local : surgery or external radiation (radiotherapy, protontherapy,...)
- Systemic : chemotherapy
- Selective systemic : targeted (nuclear medicine, immunotherapy,....)

Although the focus will be on external radiation in this context, it is crucial to remember that patients frequently receive a combination of therapies. Chemotherapy is frequently administered before radiation treatment because it increases radiosensitivity [15]. The fundamental goal of radiation, which is used in around 50% of cancer treatment regimens, is to inhibit tumor growth.

Ionizing radiation is used to treat cancer as the basic tenet of radiotherapy. These radiation types contain sufficient energy to knock electrons out of atoms or molecules. This radiation has both direct and indirect effects on DNA when it is exposed to it. Direct impacts will destroy DNA right away, while indirect effects are made possible by the radiolysis of water. Water radiolysis will result in the production of free radicals (substances with one or more single electrons). Due to these radicals' high reactivity, solutes present during irradiation may interact with them or mix with them. Free radical production is specifically influenced by the radiation's LET[1] and the presence or absence of oxygen [15]. These alterations may affect cellular functions or even cause cell death.

Radiotherapy and protontherapy damage both healthy and malignant cells. So the goal is to cure the disease by killing all cancer cells and descendants but without harming too much the patient. These two effects can be visualized in Figure 2.1 that shows the tumor control probability (TCP) and the normal tissue complication probability (NTCP) as a function of the prescribed dose).

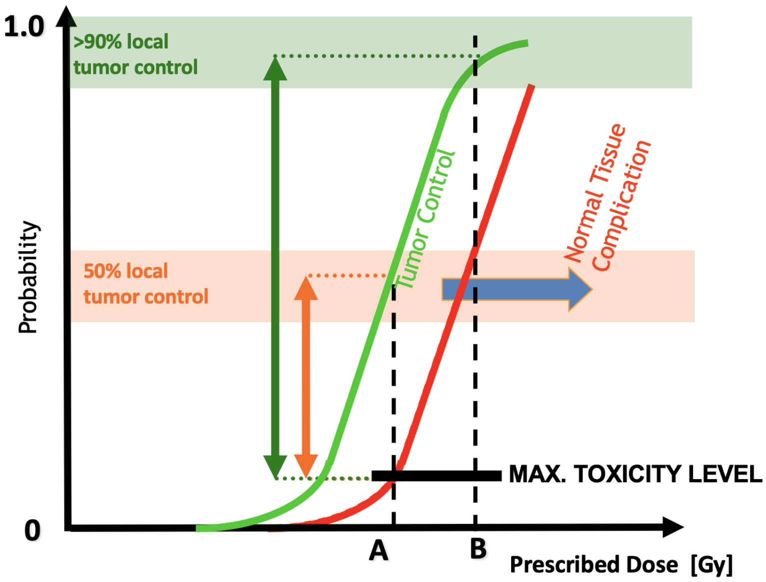

Figure 2.1: Graph representing the probability of tumor control and normal tissue complication depending on the prescribed dose [25].

The prescribed dose is a measurement of the mean energy ($\mathrm{d}\epsilon$) that ionizing radiation imparts to a mass $\mathrm{d}m$, given in Gray (Gy).

$$D = \frac{\mathrm{d}\epsilon}{\mathrm{d}m} \tag{2.1}$$

---

[1] In dosimetry, linear energy transfer (LET) is the amount of energy that an ionizing particle transfers to the material traversed per unit distance.[5]

As the prescribed dose is increased, the green curve shows how the likelihood of controlling the tumor increases, while the red curve shows how this same dose rise also causes issues in normal tissue. The possibility of controlling the tumor improves along with the dose delivered to it, but at the same time, the risk of problems in normal tissue also rises. It is quickly understood that there is a compromise between killing the tumor and preserving healthy tissues. Fortunately, there are parameters which make it possible to distance the 2 curves :

- Improved ballistics
- Better choice of particles
- Differential radiobiological effects
- Radiosensitization

We will focus on the 2 first parameters, but to quickly explain the other 2, the differential radiobiological effects are the various ways that different cells and tissues react to radiation exposure. These differences can be used to target cancer cells while sparing healthy cells and preserving sensitive tissue.

Radiosensitization is the process of making cells more sensitive to radiation therapy. This can be accomplished by administering medications or other substances that, while mostly sparing normal cells from radiation damage, render cancer cells more vulnerable to its effects. By making it feasible to deliver larger radiation doses to the tumor while sparing healthy tissue, this method can contribute to improving the effectiveness of radiation therapy.

2.1.1 Improved ballistics

Proton therapy is a type of cancer treatment that uses beams of accelerated protons to target tumors. There are two main methods for achieving the desired shape of the target volume: passively scattered proton therapy (PSPT) and Pencil Beam Scanning (PBS). PSPT uses a rotating modulation wheel and scatterers to produce a spread out Bragg peak (SOBP), while PBS uses scanning beamlets of protons to produce a more conformal and efficient dose distribution. In PBS, the treatment is delivered layer by layer for each beam energy, with the energies of beamlets defined based on the positions of spots within the target volume, and the intensities of beamlets determined using optimization techniques to achieve the desired dose distribution [20].

The dose is delivered spot by spot, with the beam turned off between points to minimize dose to healthy tissue. The energy and intensity of each pencil beam are adjusted based on the patient's anatomy and the target volume to deliver the desired dose distribution as closely as possible.

2.1.2 Better choice of particles

Protons

The dose-depth profile changes as the particle is changed, and proton treatment specifically exploits this. Protons have an entirely different dose profile than the X-rays used in conventional radiotherapy, as can be seen on the graph.

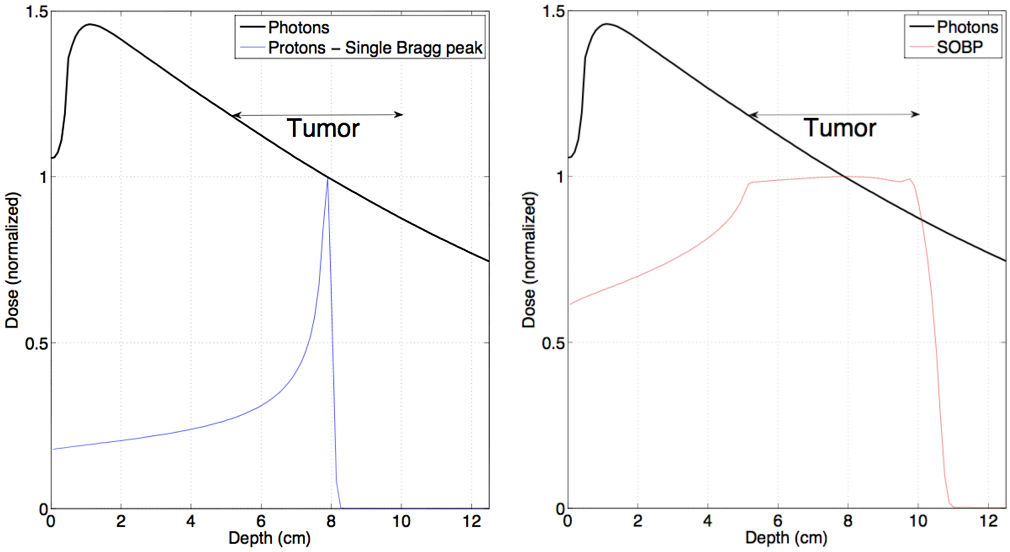

Figure 2.2: Depth-Dose profile for proton and photons [26].

As observed in Figure 2.2, the X-ray beams deposit their energy into the media shallow depth. First, there is the "build-up," during which the energy deposited in the media is at its highest before decreasing. It is immediately realized that this results in the delivery of a high dose close to the surface while tumors are generally located deeper within the body, as well as a dose beyond the tumor.

This is why protons were considered. Their dose curve ends in a maximum called "Bragg peak". This implies that one can deliver a dose in a very localized place. By varying the energy of the protons, a spread out Bragg peak (SOBP) can be created, which allows for scanning of the tumor and adjustment of its size.

Electrons

Electron therapy can have some advantages over traditional X-ray (photon) radiotherapy and proton therapy. As observed in Figure 2.3, electrons exhibit less penetration than X-rays or protons, resulting in the deposition of most of their energy within a shallow depth of the skin. This makes them well-suited for treating tumors that are located near the skin surface or in superficial body structures such as the head and neck, the breast or the skin itself at the time that protons were not available [3]. The main disadvantage of electron is the high scattering.

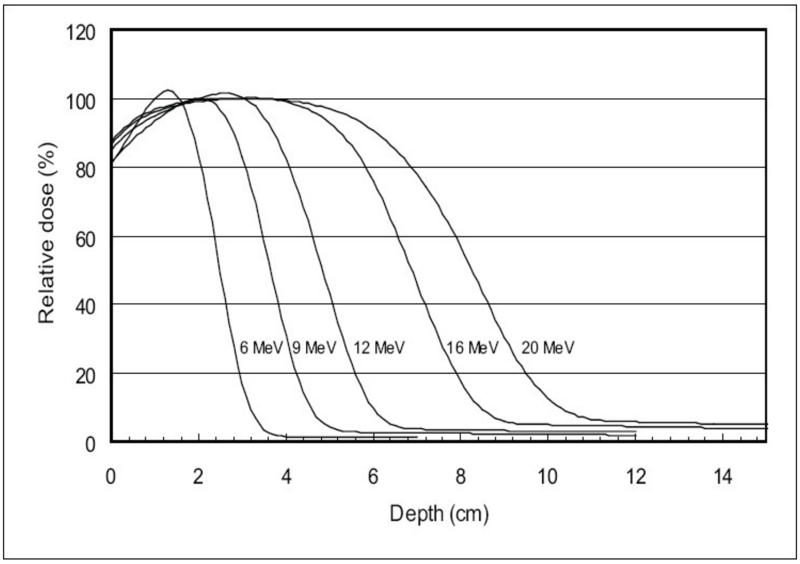

Figure 2.3: Depth-dose profile for electrons [8].

2.2 Workflow in radiation therapy

The workflow for radiation therapy consists of several phases that must be completed in order to provide the treatment. The ultimate objective is to irradiate the tumor with as little exposure to healthy tissue as possible. To do this, every workflow step must be carried out precisely and accurately to prevent treatment delivery uncertainties, which could lead to insufficient tumor elimination or excessive exposure of healthy tissue.

During the **imaging (simulation)** stage, a series of scans is performed to create a comprehensive map of the tumor and surrounding healthy tissue, which is crucial for accurate treatment planning and precise targeting of the proton beam. Computed tomography (CT) and magnetic resonance imaging (MRI) are commonly used modalities, with CT scans being mandatory for dose calculation. Additional imaging techniques like PET or SPECT may be employed to gather more details about the tumor. This imaging data is used to construct a 3D model of the tumor and surrounding tissue, and critical structures to be avoided during therapy, such as the spinal cord, are identified.

Contouring plays a vital role in the treatment planning process for proton therapy. The target volume, including the Gross Tumor Volume (GTV) representing the observable extent of the tumor, is initially determined. The GTV is then expanded according to predefined criteria to create the Clinical Target Volume (CTV), encompassing potential cancer cell regions. Organs at risk (OARs), which are neighboring organs susceptible to radiation damage, are identified and marked. The oncologist selects a prescription dose that effectively targets the tumor while limiting the maximum dose in OARs to minimize adverse effects. Accurate contouring is essential to ensure precise radiation delivery to the target while preserving healthy tissues.

2.2.1 Treatment optimization

The Treatment Planning System (TPS) is used to determine the dose distribution that will result in the body from selected incident beams. The optimum beam arrangement that will provide adequate coverage of the malignant tissues while minimizing the dose to critical normal tissues will be selected. To do this, information is required either in the form of simple external patient contours or more detailed patient image information that can be derived from computed tomography (CT) scans or other imaging modalities such as MRI. Once the beam arrangement is selected, the radiation dose is calculated throughout the volume of interest by the TPS. Having the dose distribution, the treatment planner or the physician can decide on its adequacy and determine whether further addition of beams or modification of beam direction, weighting or shaping are required to improve the treatment plan. Using such an iterative process, an optimized radiation treatment plan is developed. The TPS is further used for determining the length of time or the number of monitor units (MUs) required for each beam incident on the patient.[7]

Robust planning

One way to optimize a radiation treatment is with robust planning. In radiation therapy, robust planning is the process of developing a treatment plan for a patient that is resilient to changes in the patient's anatomy or posture throughout the course of the treatment. This is crucial because even little modifications to the patient's position or shape can have a significant impact on the dose delivered to the tumor and nearby healthy tissue. Robust planning aims to minimize radiation exposure to healthy tissue while ensuring that the patient receives the ideal radiation dosage. The optimization tries to minimize a function that takes into account setup errors, delineation uncertainties, organ motion, or range uncertainties.

2.3 Quality assurance in protontherapy

Quality assurance (QA) is a necessary process to ensure the safety and effectiveness of proton therapy treatments. The process involves a series of checks and tests designed to verify the accuracy and consistency of the proton beam delivery system and other equipment used in proton therapy. The goal of QA is to identify any problems or defects in the system before patient treatment begins, ensuring that the patient receives the prescribed dose of radiation safely and effectively.

Quality assurance encompasses three main components [9] :

- general equipment functionality,
- patient-specific quality assurance,
- treatment Planning System (TPS) quality assurance.

This thesis concentrates on the evaluation of general equipment functionality, also known as machine QA and Patient-specific QA. TPS QA will not be addressed in this context.

2.3.1 Machine QA

It is essential to guarantee the accuracy of the dose distribution delivered by the machine and predicted by the TPS. In order to build a suitable proton beam model for dose calculations, clinical commissioning entails assessing beam parameters unique to a given machine and incorporating them into the TPS. Since proton dose distributions rely on these characteristics, regular verification of them is necessary. To maintain consistent and accurate dose delivery, it is required to frequently check the equipment characteristics, the clinical data used for dose distributions, and the unit calculations.

Several categories are included in machine quality assurance (QA) techniques. One category includes dosimetry parameter checks, which track the relative dose distributions and the absolute absorbed dose to the target. Two further categories, mechanics checks and imaging system checks, assure precise placement of the target prior to dose administration. Last but not least, safety inspections concentrate on ensuring that vital equipment is operational to protect patients, workers, and visitors.

For each of these categories, these checks can be split into daily, monthly, and annual QA depending on the failure criticality of that particular check. For example, daily QA checks typically include measuring the proton beam energy, beam current, beam position, and monitoring the beam profile to ensure that the proton beam is properly aligned with the target volume. This can be done with an appropriate detector such as the IBA Sphinx Compact which consists of several flat panel (section 3.2) each with a different wedge.

Figure 2.4: Sphinx Compact detector from IBA [2].

2.3.2 Patient-Specific Quality Assurance (PSQA)

Patient-specific quality assurance (PSQA) procedures are an essential sub-component of quality assurance (QA) programs. In order to ensure treatment quality and patient safety, it must be implemented [18], as small deviations between the intended and the delivered therapy dose distributions can potentially lead to severe clinical consequences [11]. PSQA involves essential elements, such as

1. validating the treatment planning system's (TPS) capacity to accurately model the radiation dose generated by the treatment machine.
2. Confirming that the machine is capable of delivering the intended treatment.

The conventional approach for PSQA involves verifying the essential elements through phantom measurements using multi-dimensional detector arrays, as described by Johnson et al.. One commonly used detector for this purpose is the 2D ion chamber array detector MatriXX.

Figure 2.5: 2D Ion Chamber Array Detector MatriXX from IBA [1].

These measured doses are then compared to the predicted doses computed by the TPS thanks to the gamma-index. It is a quantitative metric used in proton therapy that provides a comprehensive assessment of the agreement between the measured and calculated dose distributions.

The gamma-index calculation involves comparing the dose values at corresponding points in the measured and TPS dose distributions. It takes into account both the dose difference and the distance-to-agreement (DTA) between these points. Commonly used DTA values in proton therapy range from 1 mm to 3 mm, with 2 mm being a commonly applied criterion.

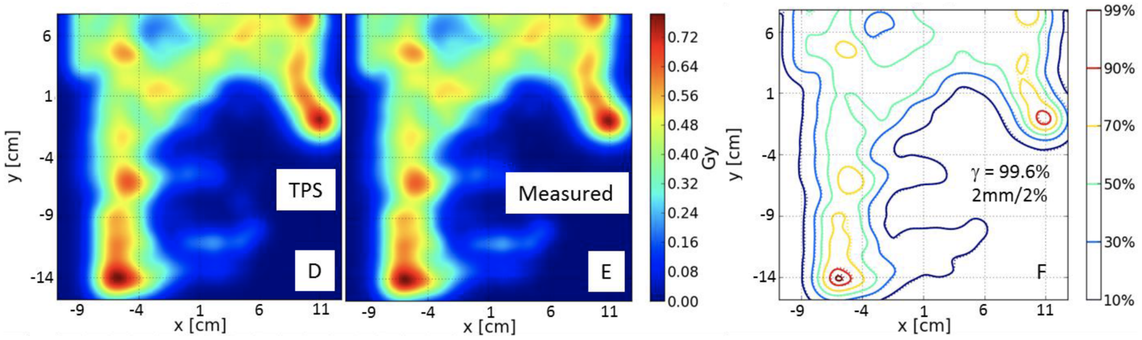

Figure 2.6: TPS-calculated (D) and measured (E) dose distributions in heat-map. (F) Isodose comparison of (D) and (E); the percentage of voxels that passed the gamma-index with a 2% dose/2mm criteria was 99.6% [29].

The process of measuring 2D dose distributions at multiple depths can be quite time-consuming, but essential when relying on measurement for quality assurance (QA) programs. The increased complexity of intensity modulated proton therapy (IMPT) plans necessitated measuring doses at greater depths to sample the complex dose distributions for each field. Even when measurements are taken at multiple depths (e.g. five depths [29]), there is no guarantee that the 3D dose distributions would be entirely suitable for treatment. Nevertheless, the probability of administering an incorrect dose diminishes as the number of verified dose distributions at different depths increases. The additional measurements not only significantly increased the measurement time, but also made the data analysis very time consuming.

Zhu et al. have reported the amount of time the treatment room was used for PSQA for 10 oropharynx patients. They estimated that the minimum time required for use of the treatment room for PSQA measurement for one oropharynx patient is about 50 min. This time including the machine settings change, set up and calibrate the detector. The limited time available for PSQA merits the development of PSQA programs that can be executed efficiently.

Independent Dose Calculation

Independent Dose Calculation (IDC) in PSQA involves performing a separate dose calculation, independent of the treatment TPS, to verify the accuracy of the TPS-calculated dose distribution.

Furthermore, instead of measuring dose distributions at multiple points, IDC performs a complete dose calculation based on the treatment plan, providing a comprehensive evaluation in a shorter timeframe.

IDC can help identify errors or discrepancies in the TPS calculations, such as inaccuracies in the beam modeling, dose algorithms, or patient-specific parameters. The plan could be rejected earlier if significant discrepancies existed between the TPS- and IDC-calculated dose distributions, assuming there was higher chance of failing the QA process. It provides an additional layer of control to catch potential errors.

Patient-Specific Quality Assurance based on Log Files

Another alternative is based on machine "log-files" and have been proposed in several works published in recent years [10, 19, 24, 29].

Logs can be used before treatment as PSQA. Compared to the usage of detectors, this method has a number of benefits. First, since no specific detector is required for the calculation of dose from log files, there is no need for calibration and there is a reduced probability of error. Second, using log files eliminates the need to set up detectors and test the dose at various stages of the treatment process, saving time and lowering PSQA costs.

The ability, combined with a Monte Carlo (MC) simulation, to calculate dose in three dimensions and in the geometry of the patient is also a major advantage of using log files for PSQA in proton therapy. Unlike detectors, which provide a limited measurement of the dose at a specific layer, log files can reconstruct the dose throughout the entire treatment volume. This provides a more accurate picture of the dose distribution and enables better assessment of the treatment efficacy and safety. Nevertheless, machine log files contain an uncertainty linked to the measurement of spot position and intensity. An error model is therefore necessary to correct logs.

Log-based PSQA can also be used after treatment to compared the delivered dose to the planned one.

Within a patient treatment plan, there exists a multitude of spots distributed across various energy layers. Each spot is characterized by a distinct spot position and MU. Consequently, utilizing an error model, it becomes feasible to retrieve the corresponding log-file uncertainty for each spot within the plan and correct it. The new plan based on log and corrected is used to recompute the actual delivered dose with an MC simulation and compared with the planned dose as seen in Figure 2.7.

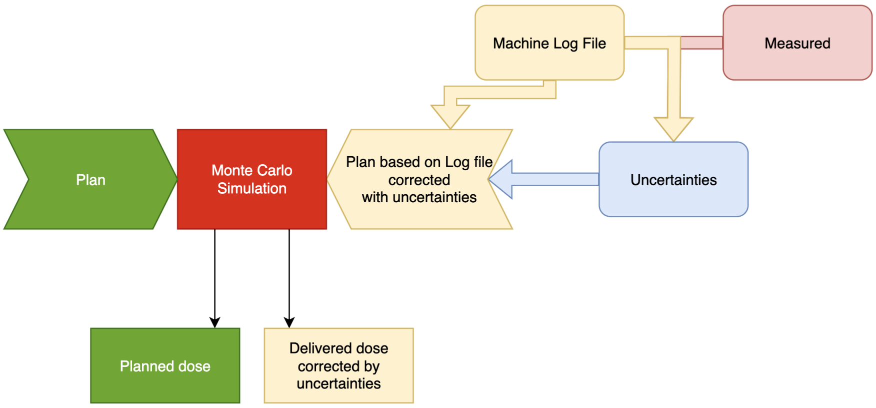

Figure 2.7: Flux diagram of the post-treatment PSQA. The spot uncertainties are calculated based on the spot given by the log and the measured one.

The purpose of this study is to take into account the uncertainties of the machine log by building an error model. Correct all the spot position and MU for a given plan with those uncertainties and combine this plan with a Monte Carlo simulation in order to compared it with the TPS.

Chapter 3

Physical concepts

In this chapter, the basics of proton transport and the different interactions with matter will be discussed. Additionally, the concept of flat panels will be explored, all in relation to the physics of proton therapy.

3.1 Interactions of protons with matter

Whether in the air, water or in patient's tissues, the proton interacts with its environment in 3 main different ways. First of all, a proton loses energy almost continuously with depth, this is due to inelastic electromagnetic interactions with the target electrons. Then, they are weakly diffused because of their large mass, this is the elastic electromagnetic and elastic nuclear interactions with the target nucleus. Finally, they are sometimes absorbed on the fly by a target nucleus which explodes immediately afterwards: inelastic nuclear reactions.

3.1.1 Inelastic electromagnetic interactions

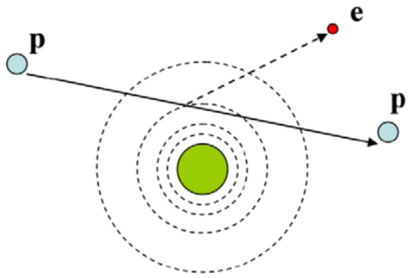

Figure 3.1: Schematic illustration of inelastic Coulombic interactions.[21]

When a proton enters the mater, he leaves a trail of ionizations and excitations along its path. Occasionally, the energy transfer is high enough to create δ-ray. This is by far the main cause of energy loss for protons. This interaction can be divided into two groups:

"Soft" collision

We said a "soft" collision occurs when a fast particle passes an atom at relatively large distance. This is the most frequent type of collision and it leads to a small energy transfer (few eV[1]) that just produces an excitation of the atomic states. As a consequence, there can be an emission of characteristic x-rays or an emission of Auger electrons. Auger electron emission is a competitive process to x-ray emission, indeed, the energy of the x-ray can also be transferred to another electron, which is ejected from the atom. This second ejected electron is called an Auger electron.

"Hard" collision

A "hard" collision is said to occur when a fast particle passes close to the atom. The energy transfer large enough to produce ionization and in some cases the electron from ionization has enough energy to produce ionization itself : a δ-ray or also called knock-on electron can be produced as a result.

After some algebra, the following formula can be obtained:

$$T_{\max} = \frac{2m_e c^2 \beta^2 \gamma^2}{1 + 2\gamma \frac{m_e}{m} + \left(\frac{m_e}{m}\right)^2} \tag{3.1}$$

where $T_{\max}$ is the maximum energy transfer, m_e the electron's mass, c the speed of light, β the is the ratio of v to c, γ the Lorentz factor and m the incident particule's mass.

We can make approximation in function of the parameters,

$$T_{\max} \approx \begin{cases} 2m_e c^2 (\gamma\beta)^2 & \text{for} \quad \gamma m_e << m \\ \gamma m c^2 = E & \text{for} \quad \gamma \to \infty \\ m_e c^2(\gamma - 1) = E - m_e c^2 & \text{for} \quad m = m_e \end{cases} \tag{3.2}$$

The only relevant choice for radiotherapy is the first case.

3.1.2 Elastic scattering

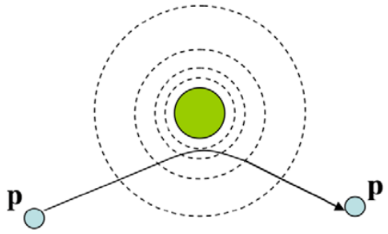

Figure 3.2: Schematic illustration of deflection of proton trajectory by repulsive Coulomb elastic scattering with nucleus.[21]

This effect is the main reason of protons' angular deflection. Indeed, most protons travel in a nearly straight line because their rest mass 1836 times greater than

---

[1] electron Volt.

electron. In contrast, a proton passing close to the atomic nucleus experiences a repulsive elastic Coulombic interaction which, owing to the large mass of the nucleus, deflects the proton from its original straight-line trajectory. During this interaction, the energy transferred to the target atom is in general negligible. However, if the target atom is Hydrogen, the transfer of energy can go up to half of the incident energy.

3.1.3 Inelastic nuclear reactions

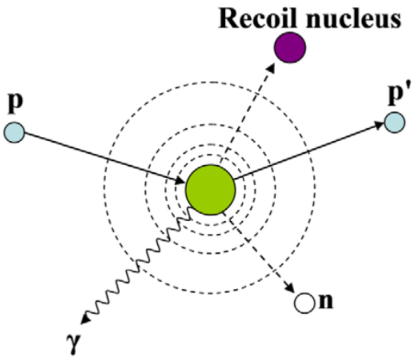

Figure 3.3: Schematic illustration of removal of primary proton and creation of secondary particles via non-elastic nuclear interaction (p: proton, e: electron, n: neutron, γ: gamma rays).[21]

In a nuclear reaction, the projectile proton enters the nucleus and the nucleus then emits a proton, deuteron and heavier ion or one or more neutrons. Non-elastic nuclear reactions between protons and the atomic nucleus are less frequent but, in terms of the fate of an individual proton, have a much more profound effect. This interaction causes an attenuation of the the primary fluence. Only protons contribute significantly to the dose at moderate distances. In radiotherapy, neutron have low relevance but have an important impact in terms of radioprotection.

Summary

Interaction type	Interaction target	Principal ejectiles	Influence on projectile	Dosimetric manifestation
Inelastic Coulomb scattering	Atomic electrons	Primary proton, ionization electrons	Quasi-continuous energy loss	Energy loss determines range in patient
Elastic Coulomb scattering	Atomic nucleus	Primary proton, recoil nucleus	Change in trajectory	Determines lateral penumbral sharpness
Non-elastic nuclear reactions	Atomic nucleus	Secondary protons and heavier ions, neutrons, and gamma rays	Removal of primary proton from beam	Primary fluence, generation of stray neutrons, generation of prompt gammas for in vivo interrogation

Table 3.1: Summary of proton interaction types, targets, ejectiles, influence on projectile, and selected dosimetric manifestations. Table taken from Newhauser and Zhang.

Finally, energy loss of protons can also occur through the Bremsstrahlung process. However, this process only becomes significant when protons reach relativistic energies, which is not applicable in the range of energies used for proton therapy.

3.2 Flat panel detector

There are various types of detectors that can be used for proton therapy quality assurance, including flat panel detectors. They provide excellent image quality, high spatial resolution and contrast, allowing for detailed analysis even if they can be more expensive compared to some other detectors. The detector used in this thesis, the Phoenix, is a flat panel. There are 2 mains flat panel detectors, the direct and the indirect.

Indirect

An indirect flat panel consists of three main components: a scintillator layer, a photodetector layer, and readout electronics.

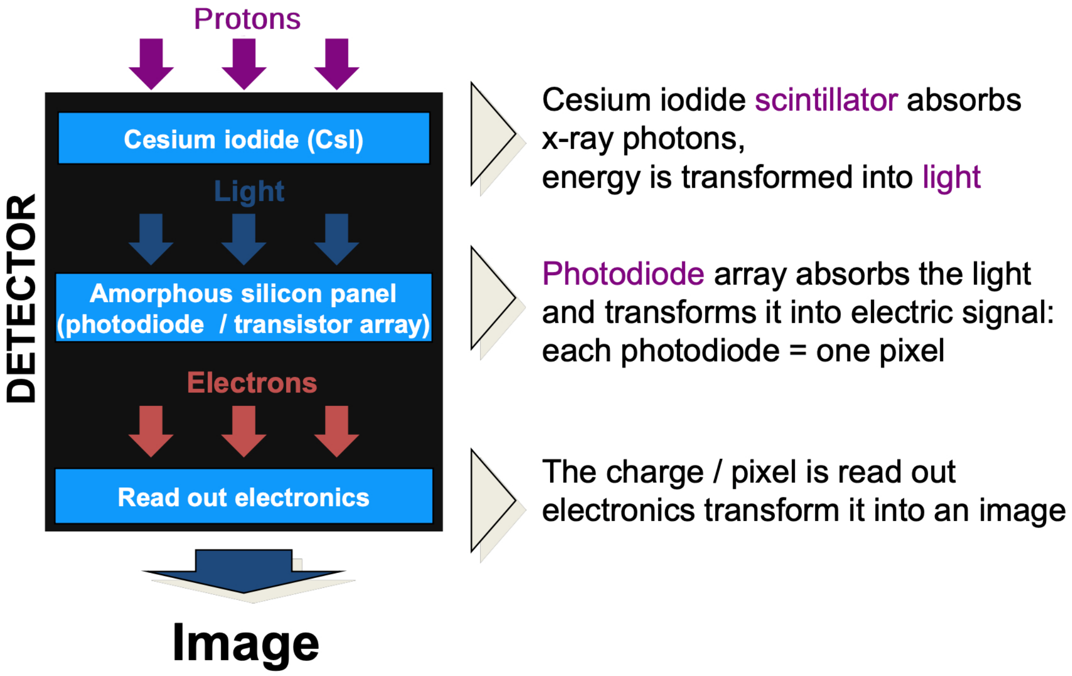

Figure 3.4: General principle: Flat Panel Detector Scintillator-based (indirect)[12].

The scintillator layer of the detector is made of a material that emits visible light when excited by ionizing radiation. This light is captured by photodiodes or other light-sensitive elements located behind the scintillator layer and by the principle of electron-hole pairs, transform it to a charge.

Many detectors use amorphous silicon (a-Si) photodiodes, each of which is an individual thin film of a-Si that is deposited on a substrate and covered with a layer of metal that serves as a cathode. The scintillator layer emits light, which is absorbed by the a-Si layer, which then produces a small electrical current that is proportionate to the brightness of the light. The charge produced by the a-Si layer is collected by the metal layer and sent to the readout circuitry.

The readout electronics of the detector are responsible for processing the electrical signals from the photodiodes and converting them into a digital image. This process involves several steps, including amplification, filtering, digitization, and reconstruction. The resulting image is a two-dimensional representation of the radiation field, with each pixel corresponding to a small area of the scintillator layer. The thin-film transistor (TFT) is a key component of the readout electronics that enables the conversion of the signals into a digital format. The TFT acts as a switch that controls the flow of current through the photodiodes.

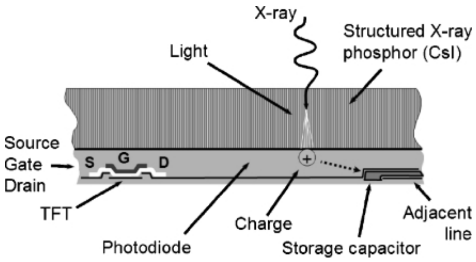

Figure 3.5: Diagram of an indirect flat panel [4].

Direct

The principle of operation of direct flat panel detectors involves the use of a photoconductive material, typically made of amorphous selenium (a-Se), which has the property of becoming more conductive when exposed to protons. The photoconductive material is sandwiched between two electrodes.

When protons pass through the photoconductive material, they are absorbed, causing an increase in the electrical conductivity of the material. This results in the formation of an electrical charge, which is collected at the pixel electrodes and read out by an integrated circuit. The electrical charge is then converted into a digital signal, which is processed to form a high-resolution image. The readout electronics are exactly the same as the indirect.

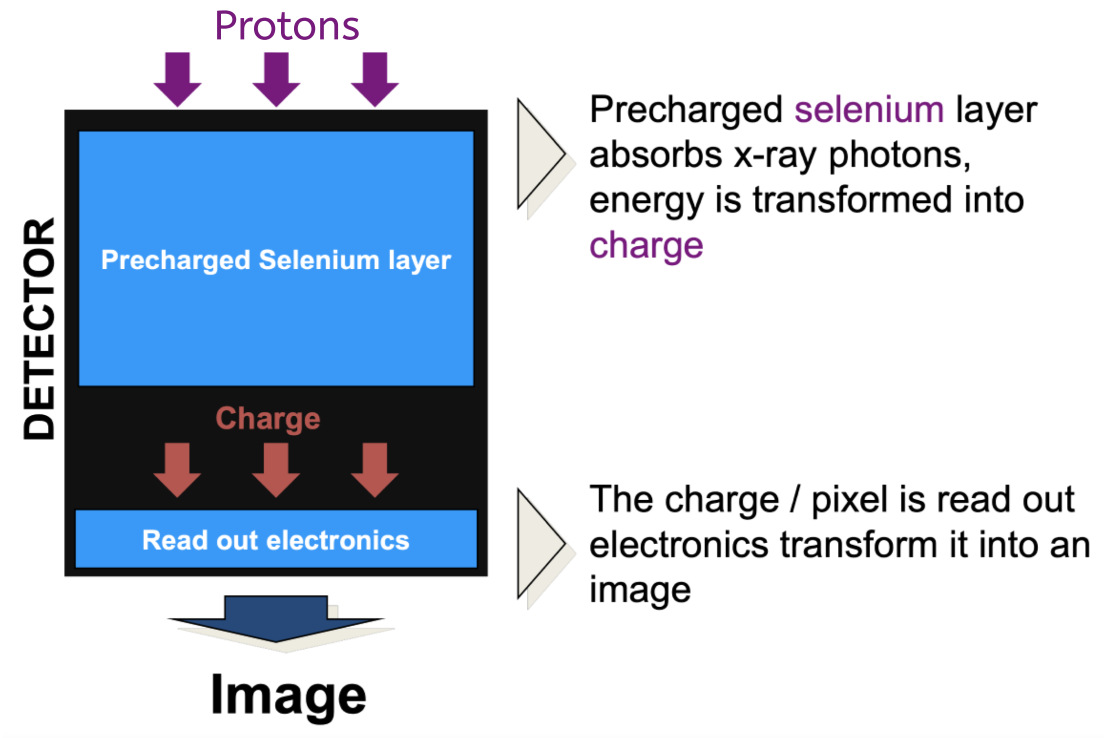

Figure 3.6: General principle: Flat Panel Detector Scintillator-based (direct)[12].

The direct flat panel detector has several advantages over indirect detectors. Since it directly converts protons into electrical charges, it does not require a scintillator layer, which can result in higher spatial resolution, less image distortion but noisy. Also, the lower number of conversion stages makes it possible to have a significantly higher conversion efficiency (~8000 direct versus 1000–2000 indirect [12]).

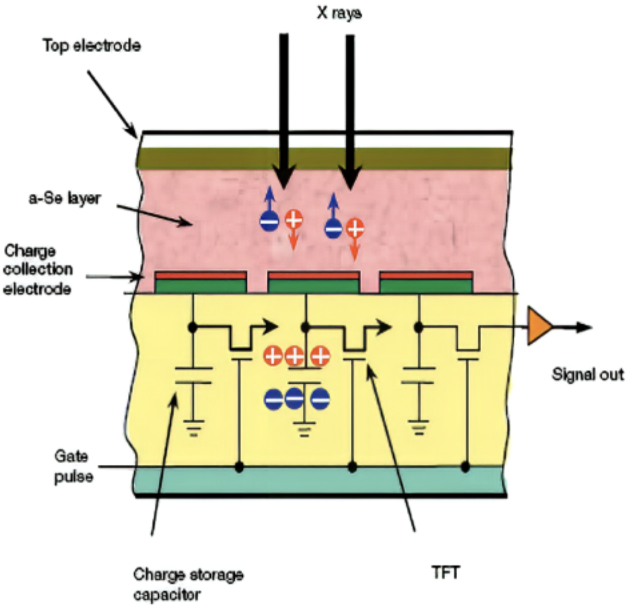

Figure 3.7: Diagram of a direct flat panel [12].

Chapter 4

Materials and methods

As said before, log carries uncertainties. The position recorded in the log file may be not exactly where protons beam go. In order to retrieve the real position of protons, we need to place a detector. A comparison can be made between the spot position measurements obtained from the treatment machine (log), external detector, and the original treatment plan to assess and characterize the deviations in log-file measurements from the actual delivery.

4.1 Materials

To acquire measurements, specific devices are required. For this purpose, a visit was made to the Universitair Medisch Centrum Groningen (UMCG) center in Groningen, the Netherlands. Investigations were carried out using a Phoenix detector from IBA Dosimetry in a proton beam produced by a cyclotron, the IBA Proteus Plus (P+) system of Groningen (UMCG). P+ enables Image-Guided Intensity Modulated Proton Therapy (IMPT) by combining the fine precision of the Pencil Beam Scanning (PBS) delivery mode [6].

4.1.1 Log-file

As a reminder, a log file is a file that store informations about the machine. For proton therapy PBS treatment, the beam position is modified by varying the current on two magnets. These two magnets bend the proton flux to scan the two orthogonal directions (x, y). In Groningen, the scanning in the X direction is made prior to Y direction.

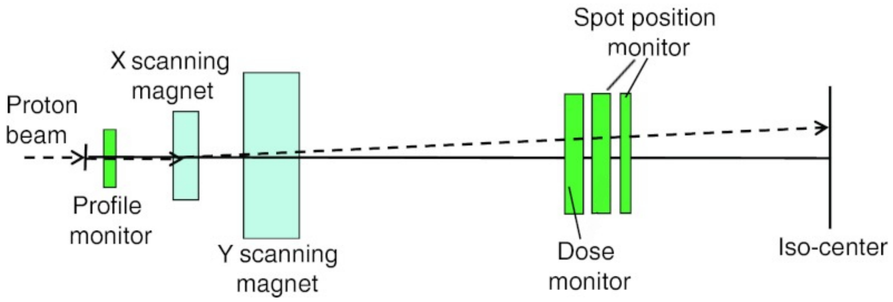

Figure 4.1: Schematic of the UMCG scanning nozzle. The proton beam is indicated by the dashed line [28].

After that, the flux passes through three ionization chambers (IC). The first one is to measure the MUs by reading-out the IC charge, because it is directly proportional to the charge. The two other ICs are composed of both horizontal and vertical strips to determine the spot position.

The spot position recorded in the machine log-files is the result of a fast Gaussian fit, which carries an uncertainty expected to be greater than the precision of the scanning system after commissioning of the current in the magnets.

Each strip in the spot position monitor collects a portion of the charge created by the proton beam. The distribution of the beam has a two-dimensional Gaussian shape when viewed perpendicular to the beam axis. As a result, each strip's signal is the integration of this Gaussian curve across the strip's surface area. The amplitude, center (x, y) and standard deviation (σ_{beam}) of the Gaussian distribution in two dimensions can be determined by fitting the measured charge distribution obtained from the two arrays of strips with an unknown Gaussian curve. The fitting algorithm iteratively adjusts the parameters of the Gaussian function until convergence is reached, indicating the best fit to the measured data. Once the fitting is complete, the parameters of the Gaussian function provide the recovered position of the beam, including the X and Y coordinates of the beam center. [13].

The recorded spot positions are then reported at the nozzle level and converted to positions at the isocenter. This transformation considers the beam divergence of the PBS scanning system [27]. The Log file gives us the spot position (X and Y) and the intensity of the beam.

4.1.2 MyQA Phoenix detector

The myQA Phoenix device consists of a 2D indirect flat panel detector (see Figure 4.3) to perform quality assurance activities on 2D high resolution Particle Therapy measurements. The active area of the myQA Phoenix device is 41 cm × 41 cm and the resolution is 0.2 mm.

Prior to taking the first picture with myQA Phoenix, the device must warm up for 10 minutes to account for internal temperature fluctuations. This background will allow to correct the measurements made afterwards.

With the range of MUs used, the gain of the detector had to be adjusted. There are up to 6 distinct gain settings supported (capacity of 0.25 pF, 0.5 pF, 1 pF, 2 pF, 4 pF, and 8 pF).The gain is changed to maximize the number of counts detected while avoiding saturation, aiming to reduce noise and increase the signal-to-noise ratio. Spot and field characteristics are unaffected by the gain value but amplitude, or count value does.

4.1.3 MyQA software

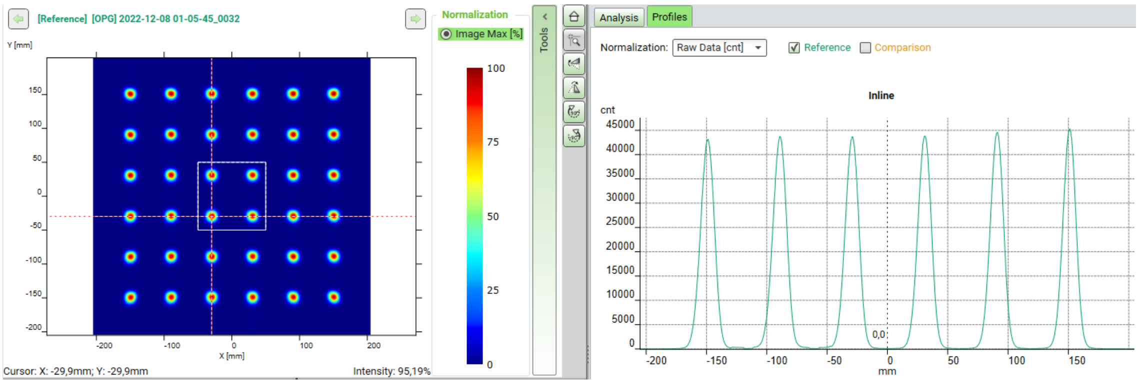

[Reference] [OPG] 2022-12-08 01-05-45_0032

Normalization: ● Image Max [%]

Normalization: Raw Data [cnt] ☑ Reference ☐ Comparison

Cursor: X: -29,9mm; Y: -29,9mm

Intensity: 95,19%

Figure 4.2: A screenshot of a part of the MyQA interface showing the spot map on the left and the profile on the right.

The myQA softwared developed by IBA Dosimetry connects with the Phoenix detector. It allows to visualize what the detector has detected. The pattern used is a 6x6 spot grid (36 spots in total) which extends at regular intervals between -150mm and 150mm in both directions (X and Y).

As can be seen in Figure 4.2, the chosen pattern is displayed, which includes the 36 spots defined in the PLD. The profile of these spots in the Y axis can be seen on the right, although both axes (X and Y) are visible. The profile is Gaussian in shape because each event is independent. The program takes us out for each spot: its position (X and Y) and its standard deviation (σ_X and σ_Y).

4.2 Methodology

This section discusses the method to compare spot position (and MU) recorded in logs with accurate spot position measurements with phoenix. The experimental mission at UMCG focused on five gantry angles (0, 45, 90, 180, and 270 degrees), six MUs (0.015, 0.1, 0.5, 1, 2, 5), and five energies (70, 100, 150, 200, and 226 MeV). The objective is to build an error model based on position between measured and log data, then use this model to better reconstruct the dose in log-based QA.

4.2.1 Acquire data

The detector was positioned on the nozzle holder and its alignment at isocenter was done using the in-room lasers (as a first approximation), as shown in Figure 4.3. Accurate alignment is necessary in order to avoid uncertainties as much as possible between the detector and the Plan. The distance to the nozzle was configured to isocenter.

An x-ray scan is performed on the detector to ensure accurate positioning since precision better than a millimeter is not feasible with laser. The back of the myQA Phoenix device includes fiducials to aid in positioning [16]. By comparing the relative positions of these fiducials to standard positions, a correction vector can be generated for all measurements at a given angle. Once the setup is complete, measurements can be taken from the control room.

Figure 4.3: The Phoenix detector is placed on a nozzle holder which is attached to the gantry. The X-ray machine can be observed below and to the right of the detector in the image.

To perform the measurements, perfect synchronization is necessary. The detection window of the Phoenix needs to be started when shooting, which is set to 10 seconds. An example of a detection window can be seen in Figure 4.2. This process is repeated five times for each angle, MU, and energy:

1. Positioning of the Phoenix and choice of the gantry angle
2. Calibrate using fiducial markers (with X-rays only when positioning the detector for the first time).
3. Set up the beam characteristics (energy, MU, angle).
4. Choose the right settings for the Phoenix and redo a background then irradiate.
5. Check if the results are correct on MyQA (no saturation, etc.).
6. If the results are good, save them in OPG on MyQA and the log file separately.
7. Repeat the process.

4.2.2 Analyse data

The objective of the error model is to account for both systematic and random errors specific to each individual spot, depending on the 3 parameters (angle, MU, energy). The model will be for the 3 datasets: Plan-Phoenix, Plan-Log, and Phoenix-Log.

Phoenix

In order to retrieve the data stored in each OPG file, groups of 5 OPGs are uploaded at a time into myQA that correspond to the same angle, MU, and energy. The resulting Excel table of 180 lines (36 spots × 5 images) is generated by the MyQA program. The average and standard deviation of the 5 images for each spot are computed, and this data is inserted into an Excel table with columns that include Angle, MU, Energy, X (spot position in X axis), Y (spot position in Y axis), stdX (standard deviation of the spot position in X axis), and stdY (standard deviation of the spot position in Y axis).

Log

To process the logs, one must first use REGGUI (MATLAB) to parse the file. The output file will be in CSV format and contain the correct number of spots (36 per image). Using a Python script, the 5 files that correspond to the same energy, angle, and MU are computed for the averages and standard deviations for each spot. The data is then saved in an Excel file with the columns: Angle, MU, Energy, X, Y, stdX, and stdY (like for the Phoenix data).

To sum up :

There are now 3 excel files, one for the data of the Phoenix detector, one for the Log-file, and one for the PLD. Each of those excel files contains 5400 lines, where each line corresponds to a spot at a given energy, MU, angle and position.

To determine the relative position between each dataset (e.g. the Phoenix and the Logs measurements), the Excel files can be subtracted from each other. This provides the Plan-Phoenix, Plan-Log, and Phoenix-Log datasets.

To construct a model of uncertainties, lookup table have been generated based on Phoenix-Log dataset, capturing the mean and standard deviation of spot position shifts at the isocenter plane. This table is based on the variations in angle, MU, energy, and spot position.

The next chapter will examine and compare the collected data.

Chapter 5

Results

Here, some of the findings from the measurements acquired will be presented. The measurements are referred to as "Phoenix" because that is the name of the detector used. The Plan is the PLD and the "Log" refers to the machine's file that was saved.

The results can be divided into groups based on angle, MU and energy, allowing us to calculate the average point position error for each parameter and observe the corresponding trends based on Σ_{ave} and σ_{ave}.

Then, an analysis of the experimental setup error will be presented and how it was measured. Finally, a point by point analysis will be performed where we will be able to draw the systematic error (Σ) and the random error (σ).

Throughout the results section, the X coordinate and Y coordinate will be analyzed separately. It is worth noting that, as shown in Figure 5.1, these coordinates correspond to the detector. The Y coordinate is tangent to the circle of rotation, while the X coordinate is parallel to the gantry's axis of rotation.

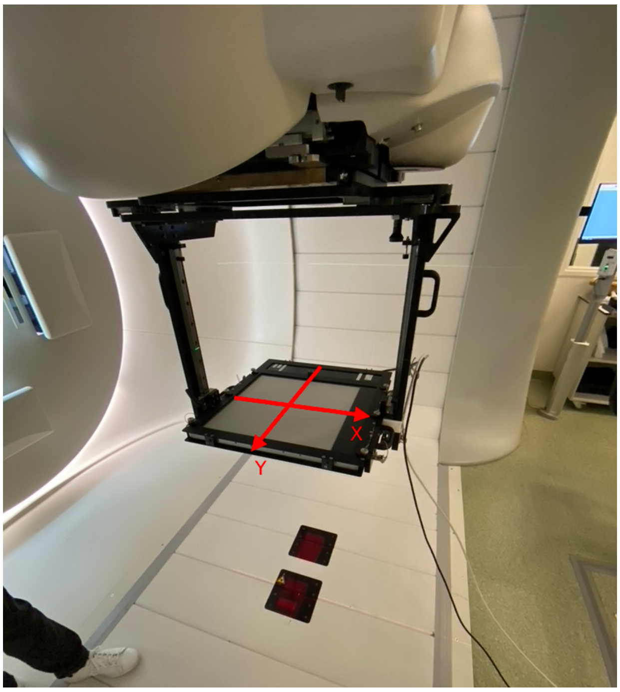

Figure 5.1: Sens of X and Y -coordinate.

The spot position difference between the Phoenix measurement, Log-recorded value, and Planned value is investigated. Based on the central limit theorem, a Gaussian distribution is expected for the difference.

The Gaussian distribution is expected to be zero-centered in the absence of systematic uncertainty. The systematic error is estimated using the mean of the distribution. Therefore, the spot position shift can be extracted as a function of parameters (Angle, MU, Energy, spot position) by comparing the spot position, and the systematic and random shift can be determined [27].

5.1 Gantry angle

In Figure 5.2, four histograms are presented, representing the spot position difference between each dataset for two angles in both the X and Y coordinates. The histograms include Plan-Log, Phoenix-Log, and Plan-Phoenix. Upon analyzing the histograms, it can be observed that the mean (Σ_{ave}) of the distribution for Plan-Log is consistently smaller than the other distributions, indicating that that the Log is consistent with the Plan.

Additionally, the sigma (σ_{ave}) of the distribution is also always smaller for Plan-Log compared to the others. Sigma is a statistical term that measures the spread of data around the mean. A smaller sigma indicates that the data is more tightly clustered around the mean, which means that the precision of the log-file is better than that of Phoenix.

Additionally, it will be investigated whether there are any differences in the data between the first and second experimental session. The angle measurement was conducted in two stages, and the investigation will determine whether the errors are more dependent on the cyclotron's performance, which may vary over time, or on the detector's placement. This difference can be explored in more detail in the subsection 5.1.1, which provides a more in-depth analysis of the data.

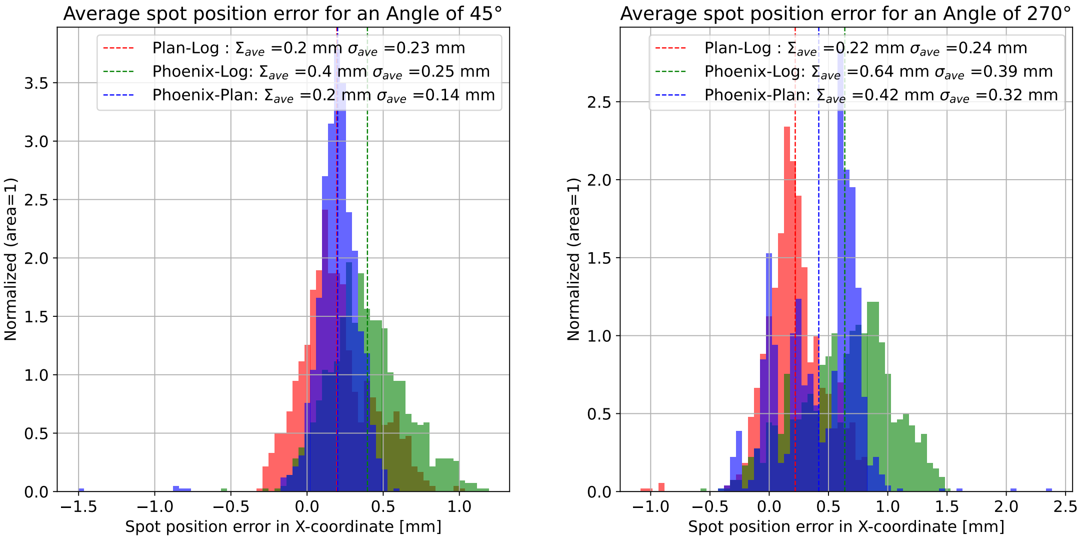

(a) X-coordinate

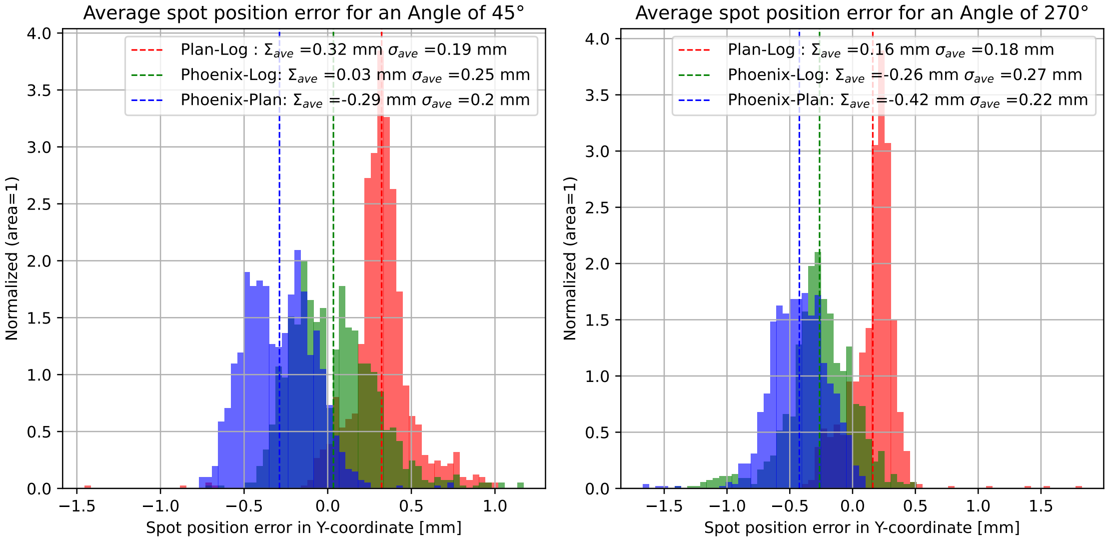

(b) Y-coordinate

Figure 5.2: 2 visualizations of the distribution for 2 energies chosen for the X and Y coordinates. Σ_{ave} represents the mean of the distribution and σ_{ave} the standard deviation of the distribution.

The data for all angles can be displayed in the form of bar plots (Figure 5.3) to gain a better understanding of the impact of the angle on the average spot position error. By comparing the mean and standard deviation of the error for each angle, patterns or trends in the data can be identified.

The y-axis can be used to display the mean of the spot position difference, while the x-axis can be used to show the angles. In each plot, the standard deviation of the distribution can also be shown as error bars. This will display a graphical representation of the average random error associated with each angle.

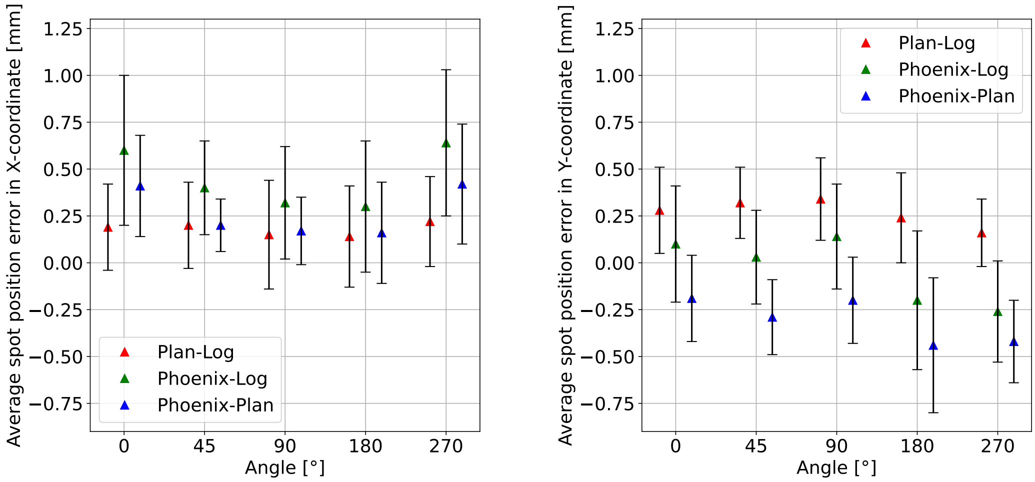

Figure 5.3: Plot of the average difference depending on the gantry angle for X and Y coordinate (resp. left and right) for the 3 datasets. Triangles are representing the mean error and the whiskers extend for the standard deviation.

For X-coordinate

It is important to remember that the detector's X-coordinate is collinear to the gantry's axis of rotation. As observed in Figure 5.3, the errors in radiation treatment showed variations depending on the angle of the gantry. A decrease in differences was noticed up to a 180° angle, followed by an increase for all the data. This reduction in differences at 180° is most likely due to the weight of the gantry, notably the arm through which the protons flow, which moves the machine's center of mass. The arm is positioned lower while the gantry is at 180°, resulting in this effect.

Another notable finding is that differences stay steady between 90° and 180° (4th quadrant) and 270° to 0° (second quadrant), i.e. opposite quadrants. The differences change until the passage of the angle, which induces an exterior radial component for 90-180° and an interior radial component for 270-0°. Overall, the average error does not exceed 0.64 mm according to the X coordinate

For Y-coordinate

It can be observed that the Log data is more affected by changes in the Y coordinate than in the X coordinate. This effect is most pronounced at the 90° angle and decreases to a minimum at the opposite angle, 270°. This trend could be influenced by the weight of the gantry.

In contrast, for the detector data, the differences are consistently negative, with no clear pattern but variations among angles. The reason for these variations will be investigated in the next section. However, despite the variations, the average error remains within 0.26mm.

5.1.1 Difference between experimental session 1 and 2

Further exploration of the data is required to identify the origins of errors for each angle. First, let's focus on the 'Plan-Log' and 'Phoenix-Plan' datasets to separate the error coming from the cyclotron and the detector. The graph of barplots shown in Figure 5.3 can be decomposed by energies to gain a better understanding of the results.

Starting with the 'Plan-Log' dataset, the accuracy for the X coordinate is observed to be good, but for Y coordinate, it is not as accurate as seen in the Figure 5.4.

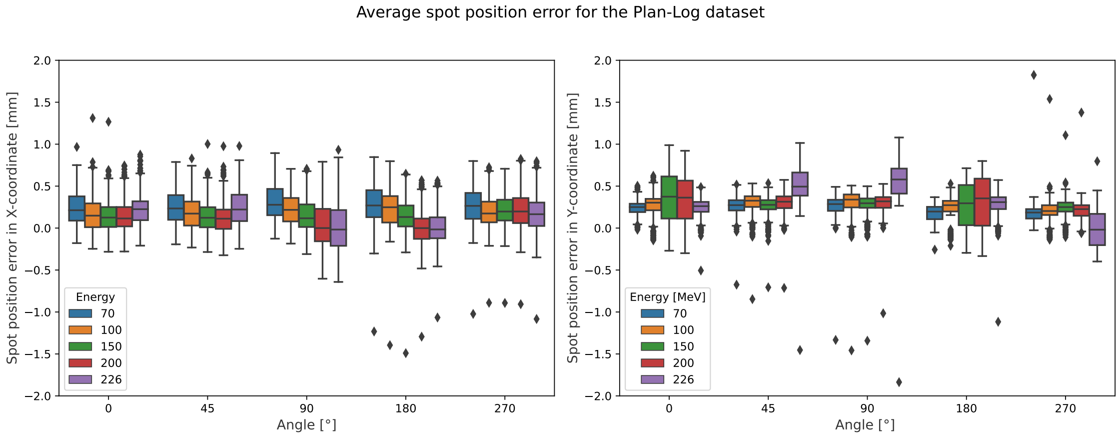

Figure 5.4: Average spot position error for Plan-Log data set as a function of the angle and energy. The box represents the interquartile range (IQR), which is the range between the first quartile (Q1) and the third quartile (Q3). The line inside the box represents the median. The whiskers extend from the box to indicate the range of the data. They can be calculated as 1.5 times the IQR. Any data points that fall beyond the whiskers are considered outliers and are plotted as points.

It was found that the accuracy of the X-coordinate is better than that of the Y-coordinate. Additionally, when decomposing the barplot by energy for the 'Plan-Log' dataset, it was observed that the spread for the X-coordinate is higher for angles 90° and 180°. This was found to be due to a decrease in spot position error while increasing the energy, while the other angles remained precise.

Regarding the Y-coordinate, it was observed that the spread of the average spot position error is greater for energies of 150 and 200 MeV for 0° and 180° angles. However, the systematic error remains consistent with the other energies for these angles. Additionally, the variation in spot position error for the Y-coordinate is due only to the 226 MeV energy. The energy of 226 MeV is the maximum that the cyclotron can deliver and it is not difficult to calibrate it to the other energies.

Interestingly, the variation for the 226 MeV energy is positive for the 45° and 90° angles but negative for the opposite angle of 270°.

It can be concluded that there was no difference between the first experimental session and the second for the Plan-Log dataset, indicating that the cyclotron delivered the same way and there was no variation on this side.

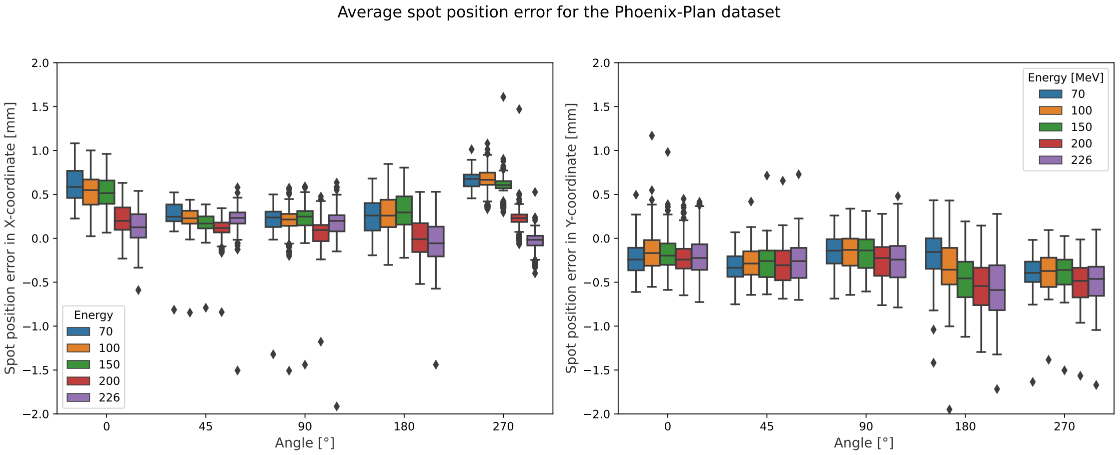

Figure 5.5: Average spot position error for Phoenix-Log data set as a function of the angle and energy. The box represents the interquartile range (IQR), which is the range between the first quartile (Q1) and the third quartile (Q3). The line inside the box represents the median. The whiskers extend from the box to indicate the range of the data. They can be calculated as 1.5 times the IQR. Any data points that fall beyond the whiskers are considered outliers and are plotted as points.

Based on the figure Figure 5.5, several conclusions can be drawn regarding the accuracy of the dataset 'Phoenix-Plan'.

For the Y-coordinate, the difference is stable for most angles, except for the 180° angle, where increasing energy leads to a decrease in error. On the other hand, the X-coordinate shows more variability. This analysis reveals that the 0° and 180° angles have a higher standard deviation, indicating a more widely distributed range of errors, for the 'Phoenix-Plan' dataset. Meanwhile, the 45° and 90° angles appear to be the most precise and stable. Additionally, the 270° angle seems to be even more precise, but the decomposition highlights that the error in spot position largely depends on the energy used.

It can be concluded that there is no significant difference between the first session and the second for the Phoenix-Plan dataset. However, as observed, there are notable variations for each angle, indicating that not only positioning (translation) but also rotation correction are crucial.

5.1.2 Detector position

At each angle, the calculation of the translation and rotation correction vector was performed. Each measurement has been corrected to remove as much as possible the uncertainties related to the positioning. At each positioning of the detector, an X-ray image was made to compare the positions of the fiducials with their real coordinates. In addition, a plumb is installed to correct the rotation of the detector. At the time, the positioning error of the markers was estimated at 0.1 mm according to IBA Dosimetry. Unfortunately, it turned out to be much larger.

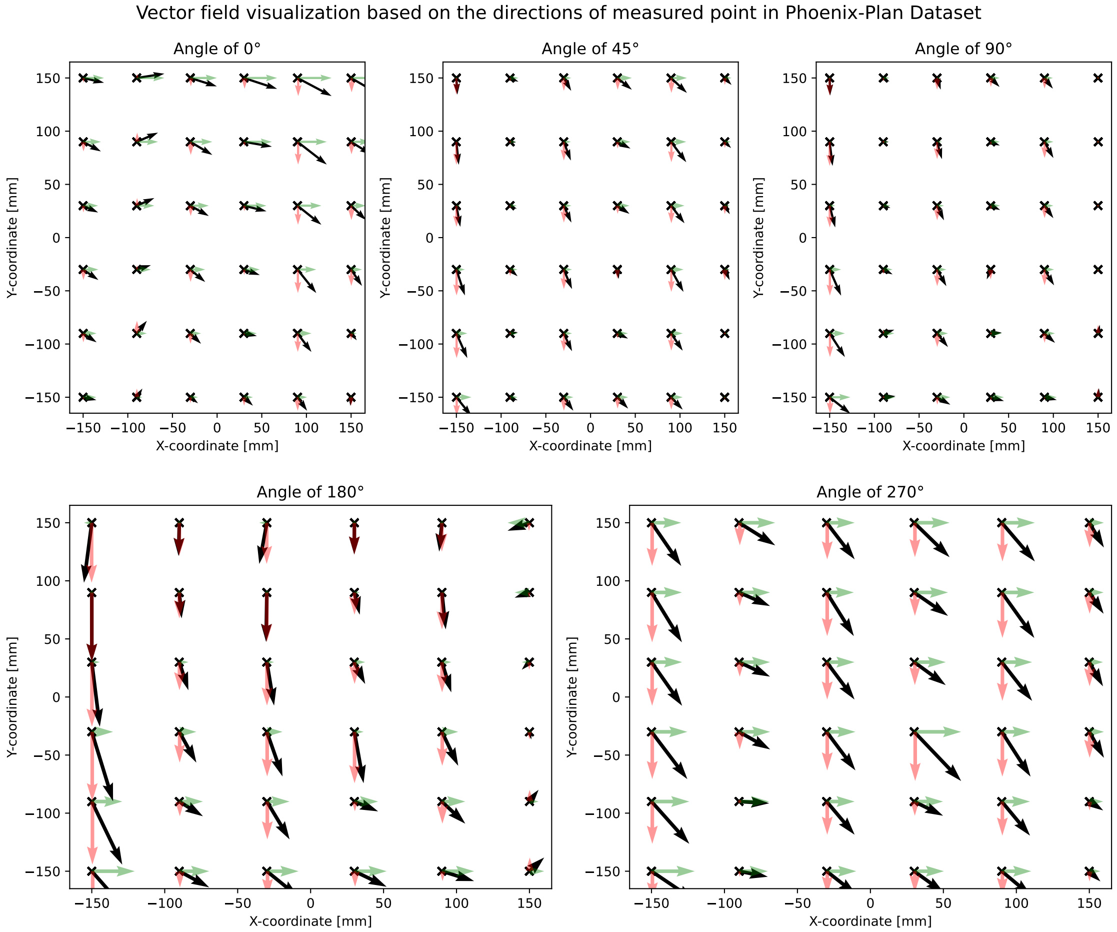

Figure 5.6: Vector field representing the average direction of the measured points with respect to the planned ones for each angle. The green and red arrow are respectively the decomposition in the X and Y coordinate.

Each arrow corresponds to the direction of the measured point compared to the target point. All together they can form a vector field that shows the "dynamic". All vector fields have already undergone correction. Upon examination of the results, a noticeable rotation in the vector field was observed for the 0° and 180° angles. This means that the rotation results in a larger systematic error and spread, which is a logical outcome. However, for the remaining three angles (45°, 90°, and 270°), there is no direct sign of rotation, only translation.

5.2 Monitor Unit (MU)

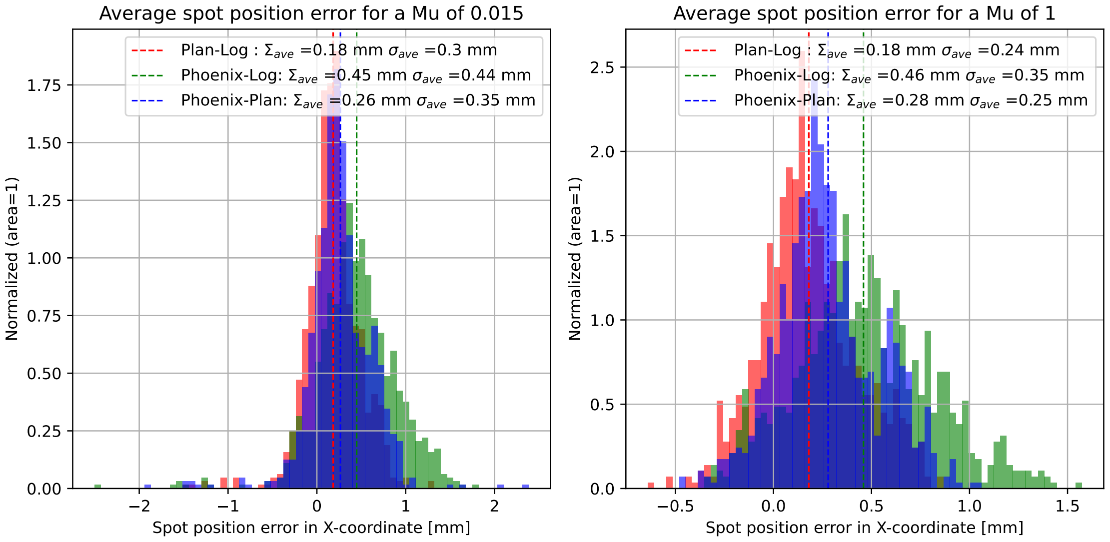

(a) X-coordinate

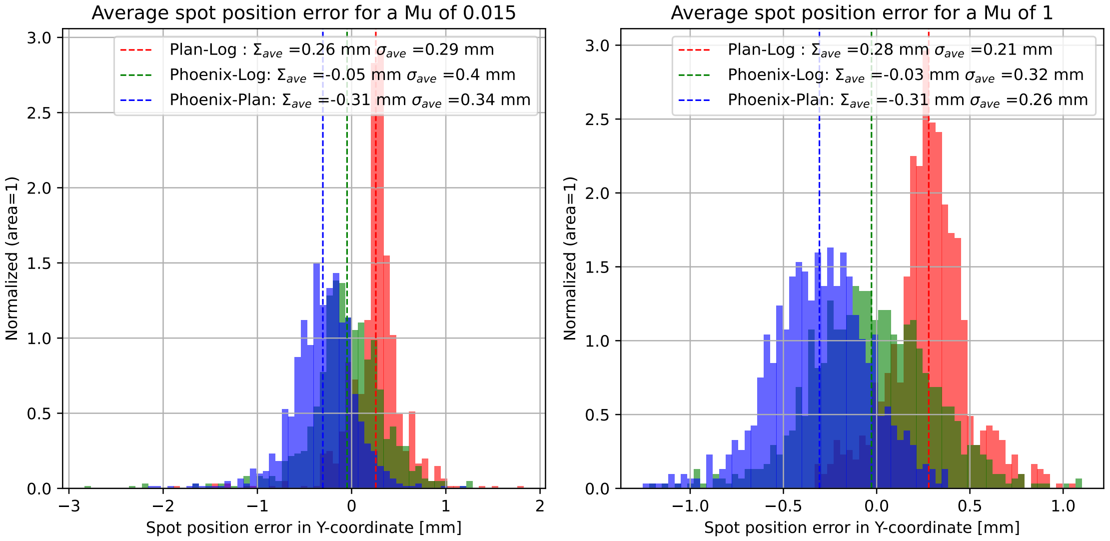

(b) Y-coordinate

Figure 5.7: 2 visualizations of the distribution for 2 energies chosen for the X and Y coordinates. Σ_{ave} represents the mean of the distribution and σ_{ave} the standard deviation of the distribution.

For both X and Y coordinate, it seems that there aren't a trend between MUs and the spot error position as it remains constant. Nevertheless, on average, the high MUs have a smaller spread. As observed for the impact of the angle, the Plan-Log is still very precise.

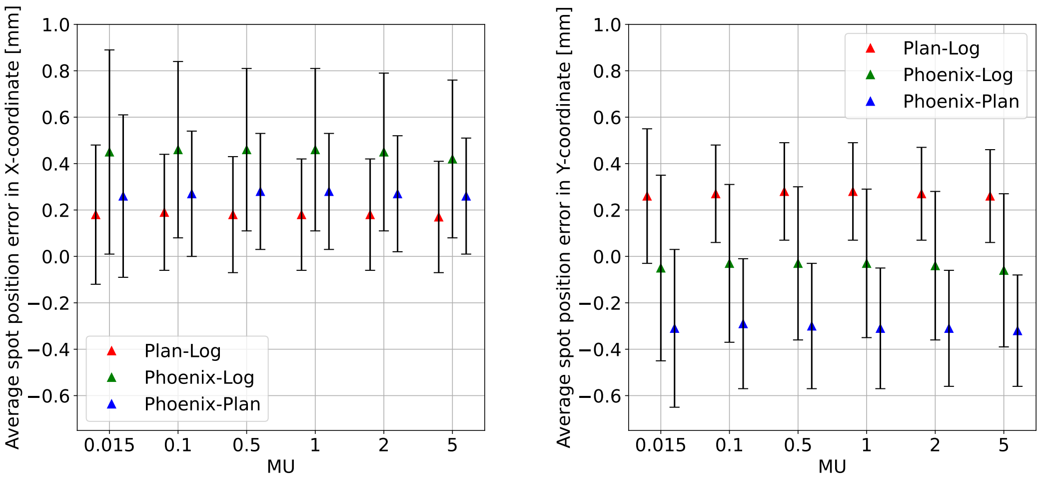

Figure 5.8: Plot of the average difference depending on the gantry angle for X and Y coordinate (resp. left and right) for the 3 datasets. Triangles are representing the mean error and the whiskers extend for the standard deviation.

The analysis of the spot position error data against monitor unit (MU) reveals some interesting trends. Firstly, the average spot position error is found to be consistent across all the data sets, indicating a high degree of accuracy in the delivery. Upon closer examination, it is observed that the error tends to increase from 0.015 to 0.1 MU, after which it remains constant from 0.015 to 2 MU. Notably, the difference slightly decreases at 5 MU for both X and Y coordinates. Overall, the average systematic error don't exceed 0.45mm and 0.06mm in X and Y coordinate respectively.

In addition to the average spot position error, the spread (σ_{ave}) of the Gaussian distribution was also investigated. The spread error reduced slowly as the MU grew for both the X and Y coordinates. These data imply that the monitor unit has little effect on the accuracy of spot location measurement, which confirm what Toscano et al. already reported.

5.2.1 True Mu

This subsection will analyze the discrepancy between the intended and actual monitor units (MU) provided to the patient, so Plan-Log dataset. As previously stated, the MU values are calculated using an IC in the nozzle . To summarize, the monitor unit quantifies the dose supplied to a patient during a therapy session. It is a dosage unit similar to the gray scale (Gy).

MU	0.015	0.1	0.5	1	2	5
Mean error	-1.8e-05	0.00031	0.001712	0.001749	0.001575	0.001424
Error [%]	0.12	0.31	0.34	0.17	0.078	0.02

Table 5.1: Mean error and percentage of error for each MU based on the Plan-Log dataset for all gantry angles and energies.

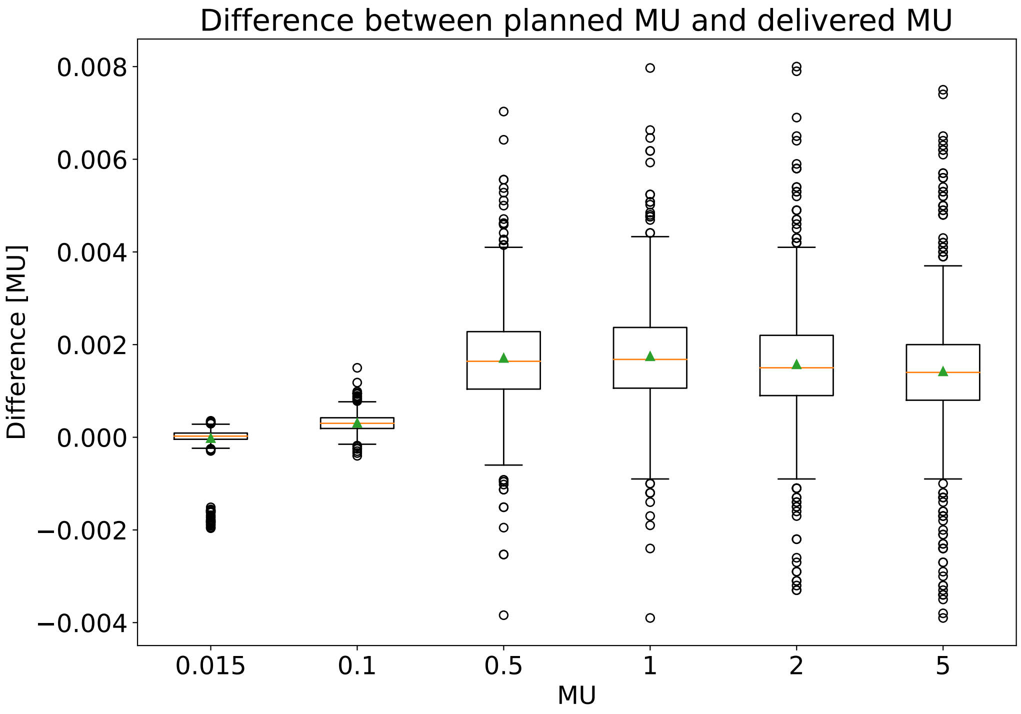

Figure 5.9: Difference between wanted MU from Plan and true MU from Log-file. The green triangle represents the mean error. The box represents the interquartile range (IQR), which is the range between the first quartile (Q1) and the third quartile (Q3). The line inside the box represents the median. The whiskers extend from the box to indicate the range of the data. They can be calculated as 1.5 times the IQR. Any data points that fall beyond the whiskers are considered outliers and are plotted as points.

Figure 5.9 displays the distributions based on the desired monitor unit (MU), while Table 5.1 shows the corresponding average values and percentage errors relative to the desired MU for all gantry angle and energy. Log measurements closely match the requested values for small MUs (0.015, 0.1), while the measurements for MUs between 0.5 and 5 are slightly off. However, when considering the errors as a percentage, MU=0.5 exhibits the largest average difference.

The desired MU can be obtained not only from the Log file and the Plan, but also from the Phoenix detector. However, it should be noted that the Phoenix detector uses multiple gain factors to prevent saturation at high MU and energies, and there is no available information on the associated errors with each gain. Therefore, a direct comparison between the measurements obtained from the Phoenix detector and those from the Log and Plan may not be accurate. It is essential to explore this further to determine whether the MU values have a significant impact on the position errors and the accuracy of the MU measurements.

5.3 Energy

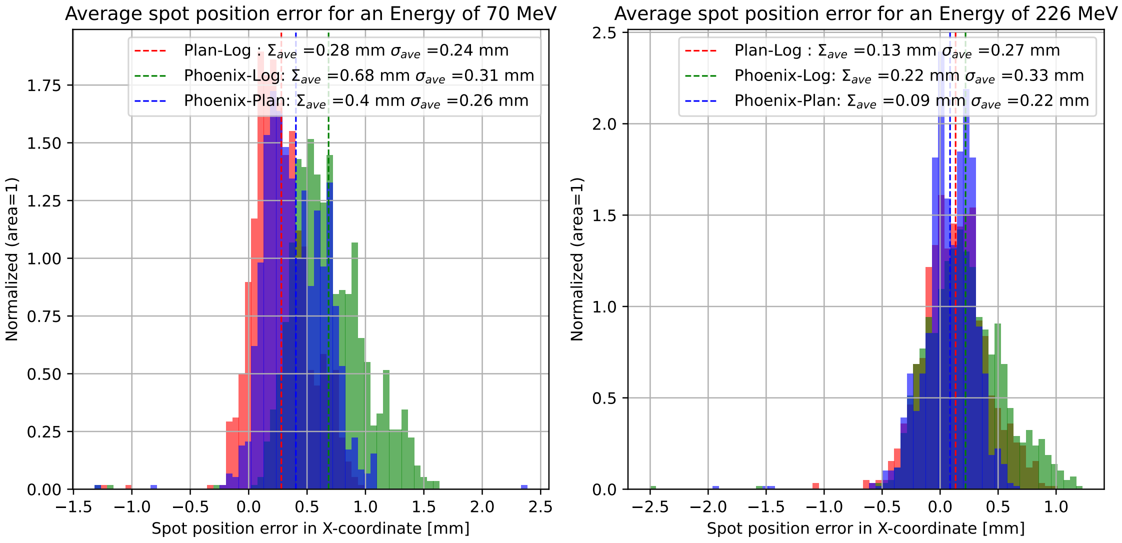

(a) X-coordinate

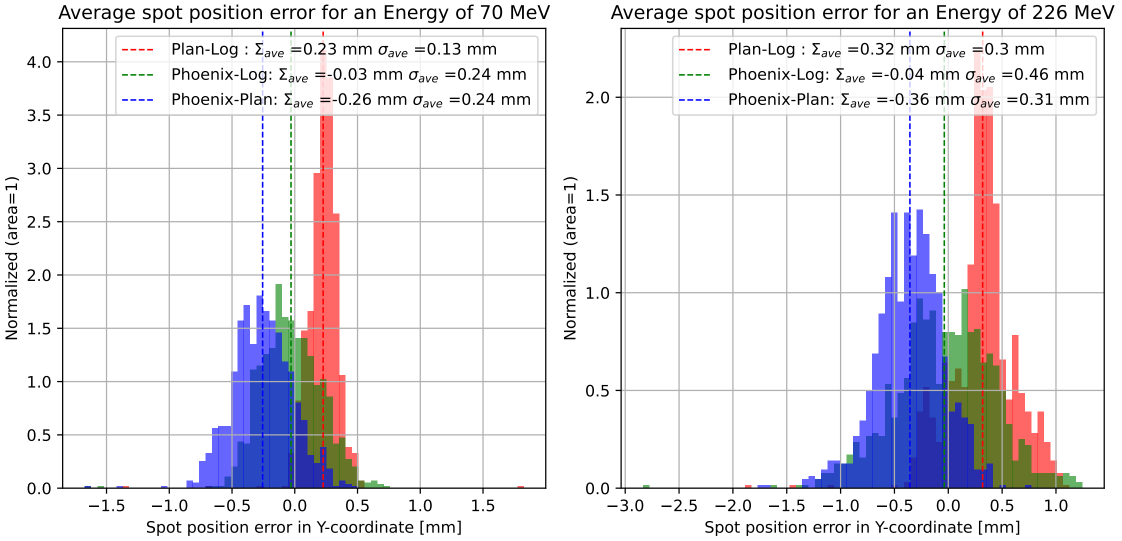

(b) Y-coordinate

Figure 5.10: 2 visualizations of the distribution for 2 energies chosen for the X and Y coordinates. Σ_{ave} represents the mean of the distribution and σ_{ave} the standard deviation of the distribution.

Based on the histogram presented above, two trends can be observed. Firstly, at high energy, the spot position error appears to be lower in the X coordinate but higher for the Y coordinate. Additionally, it can be observed that higher energy levels result in an increase in outliers in the data sets, with a corresponding increase in deviation.

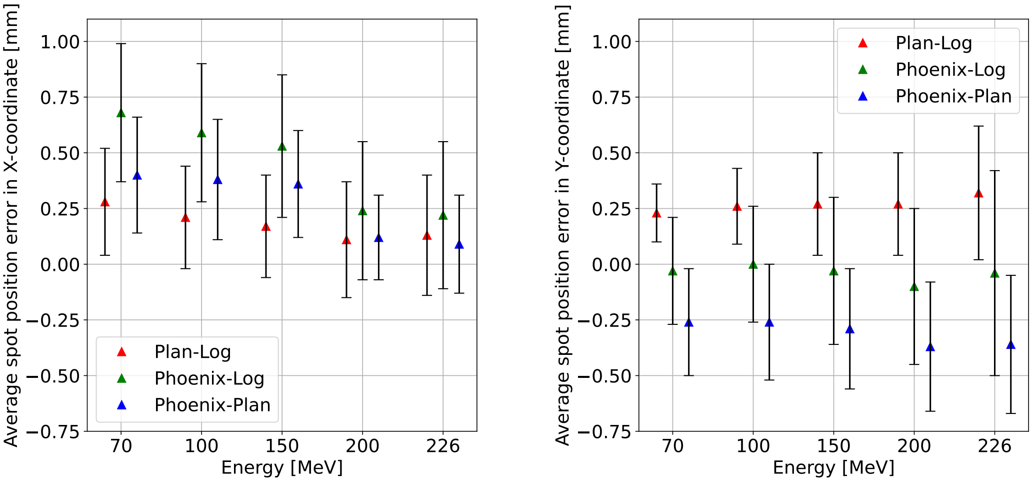

Figure 5.11: Plot of the average difference depending on the gantry angle for X and Y coordinate (resp. left and right) for the 3 datasets. Triangles are representing the mean error and the whiskers extend for the standard deviation.

By looking at the barpots, the trends in the average spot position errors in the X and Y coordinates are confirmed. In the X coordinate, the average spot position error decreases as the energy increases and so for all data sets. However, in the Y coordinate it is exactly the opposite, the Phoenix-Plan and Plan-Log position errors increase as the energy increases.

One hypothesis comes from the scanning magnets. In order to create a scanning pencil beam, the beam is deflected using two magnets—one for the X coordinate and one for the Y coordinate. The scanning can be performed by adjusting the X coordinate first and then the Y coordinate. However, this method may result in faster variations in the Y coordinate, leading to more errors as the energy increases.

Another possibility is related to the strip detector. If the beam hits a strip directly, it can result in a inaccurate Gaussian fit, which is used to interpolate the position.

Furthermore, for the Phoenix-Plan data set, a considerable reduction is observed in position error between energies of 150 and 200 MeV. This due to the spot size that is bigger at low energy because of the scattering. Also, the error in the X coordinate for the Phoenix-Plan data set is less than the Plan-Log data set at 226 MeV while being twice as big for energies 100 and 150 MeV.

Concerning the spread, at all energy levels there is no change in the average random spot position error in the X coordinate. But in the Y coordinate, the difference remains constant from 70 to 200 MeV and increases at 226 MeV.

In conclusion, based on the analysis of the average data for each parameter, it can be concluded that the impact of MUs on spot position error variation is small, if not negligible. As these errors are constant for the range of MU going from 0.015 to 5 MU, it is easy to characterize them and to take into account their impact. The energies have an impact on the errors but that depends on the coordinate. It has been observed that errors decrease with high energies for X coordinate, but they incread for Y coordinate. Finally, gantry angles play an important role in errors but can also be characterized because of the gantry weight, at least for the X coordinate. In general, each angle induces slight movements of the detector and so require new calculations for correction. If the corrections are not well corrected, this leads to large variations in errors.

5.4 Experimental error

In order to quantify the experimental setup error, dedicated measurements were performed. One angle, two energies, and two MUs values were selected for the measurements. The first measurement was taken on the first experimental session for 0 and 45 degree angles. The other two measurements were taken on the second session after removing the detector, putting it back in place, and taking the exact same measurements. This process was repeated twice.

Here are the results of the "3 setups". The setup1 is the one made the first experimental session and the two others the second session

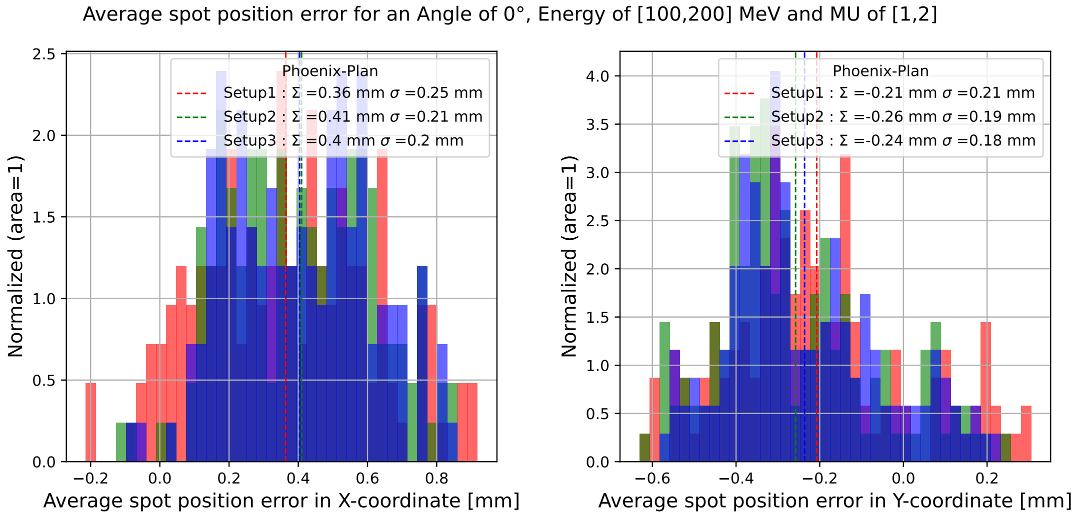

Figure 5.12: Experimental error on our measurements.

On average, the experimental setup error appears to be similar for both X and Y coordinates. The inaccuracy ranges from 0.36 to 0.4 mm in the X coordinate and from 0.21 to 0.24 mm in the Y coordinate.

Additionally, by examining the distribution of the data, the first session's measurement was slightly more precise even if the spread is larger.

This can be due to different parameters such as detector tilt and rotation, X-ray imaging or fiducials selection and their positions giving a wrong correction vector. The fiducials selection hypothesis can be ruled out because the selection of the fiducials was done randomly for each new placement of the detector.

Correction	X-coordinate [mm]	Y-coordinate [mm]	Rotation [°]
Setup1	-0.12	1.13	-0.15
Setup2	-1.1	0.45	0.07
Setup3	0.02	0.91	0.11

Table 5.2: Correction vector and rotational applied to the data.

But this is only on average, let see this spot by spot.

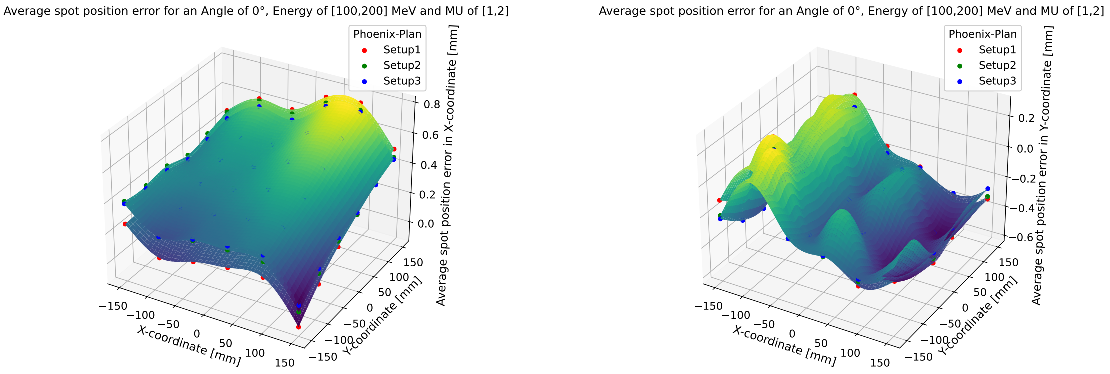

(a) X-coordinate

(b) Y-coordinate

Figure 5.13: Average spot position error for the 3 setup. The average of each spot was made for energies of 100 and 200 MeV, MUs of 1 and 2, angle of 0°.

It can be observed that the data points form a smooth surface in the X coordinate that resembles a plan. An interesting finding is that there is a decrease in error for the edge at 150mm in X. It is noteworthy that one row around X$= 90-30$mm before this edge shows additional error before this decrease.

The surface is bumpier in the Y coordinate. The surface has a wave-like appearance. There aren't three points that are successively higher and lower than one another. There is a significant decline at X$= -150$mm.

Interestingly, a distinction can be made between the first and second experimental session (where "setup1" refers to the first and "setup2" and "setup3" refer to the second). The surface of setup2 and setup3 are superimposed, but the surface of setup1 is slightly tilted. Despite the detector being removed and replaced before each measurement, it is observed that the detector was positioned almost identically for setup2 and setup3, which were taken on the second experimental session.

Furthermore, it can be observed that all three setups produce identical surfaces for the X and Y coordinates, except for the tilt. This tilt in the surface is caused by a rotation in the X-Y plane of the detector, as shown in Figure 5.14. Therefore, a rotation of the detector leads to a tilt in the 3D graph, while a translation in the X-Y plane results in a translation in the Z-axis in the 3D graph.

If there was no rotation, the surface would be flat (with the exception of bumps caused by the detector's reaction) and if there was no translation, the systematic shift (Z-axis) would be equal to 0.

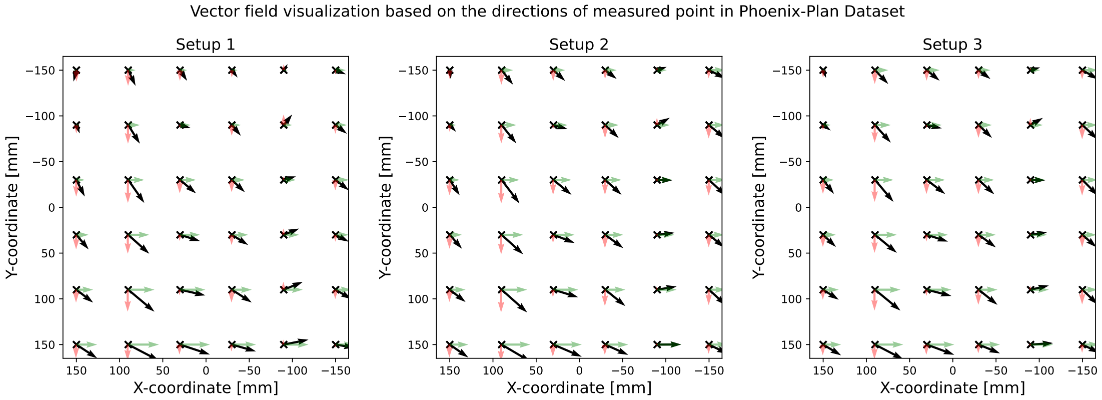

Figure 5.14: Vector field representing the average direction of the measured points with respect to the planned ones for the 3 setup. The green and red arrow are respectively the decomposition in the X and Y coordinate.

5.5 Interpolation

Having examined the average impact of each parameter on the spot position error, it is now necessary to conduct a closer inspection of each individual spot.

The interpolation of uncertainties has been performed for all five parameters, which encompass the X and Y coordinates, the MUs, energies, and angles. One crucial aspect of the angle parameter is its cyclicity, where the 360° angle must be the same as the 0° angle.

Each surface presented below represents the systematic error in X for a single angle, energy, and MU. Similar surface for the Y coordinate can be made. The base angle of 0°, MU of 1, and energy of 200 MeV was selected for comparison.

Gantry angle

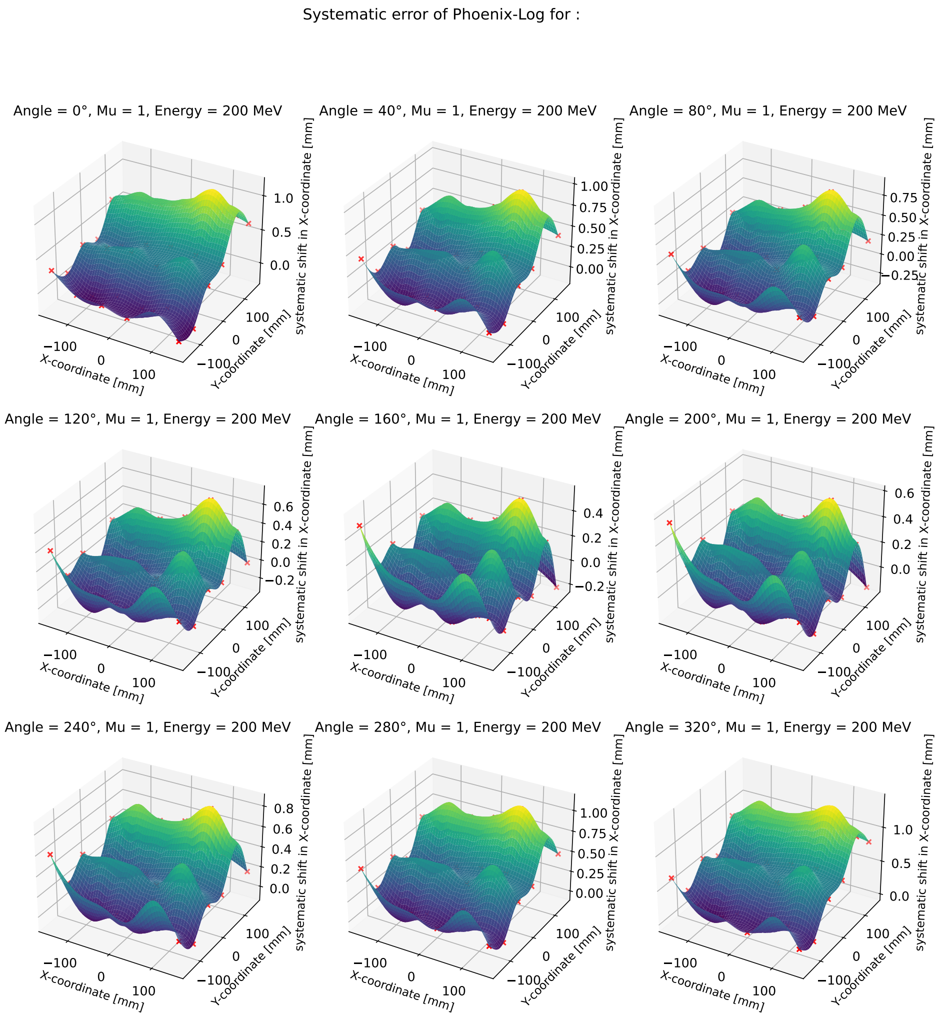

Figure 5.15: Evolution of the systematic error spot by spot in the X coordinate against gantry angles.

Based on the figures above, several observations can be drawn regarding the systematic error of the dataset. It is observed that the systematic error is dependent on the angle. The systematic error for the Phoenix-Log dataset is highly dependent on the positioning of the detector and the corrections made, including translational and rotational corrections made for each angle. On the other hand, in Appendix A, it can be observed that the Plan-Log dataset produces a surface of error that does not vary significantly with angle, indicating the importance of detector placement.

In addition, the bumps in the surface come from the Log dataset, as seen in Appendix A, where the errors in the X-coordinate give rise to a smooth surface. One possible explanation for these bumps is the presence of a strip located in the nozzle. When the measurement is taken at the exact location of a strip, the fast Gaussian interpolation method used to calculate the position cannot interpolate properly, leading to increased error.

Finally, notice that the surface for the Phoenix-Log dataset is not tilted from 90 to 270° angle, as the contribution of the tilt from the Phoenix-Plan dataset in Appendix A is opposite to that of the Plan-Log dataset in Appendix B, cancelling each other out.

Random error have also been investigated and can reach -0.08mm in X coordinate and -0.06mm in Y coordinate. No pattern have been found.

Monitor Unit

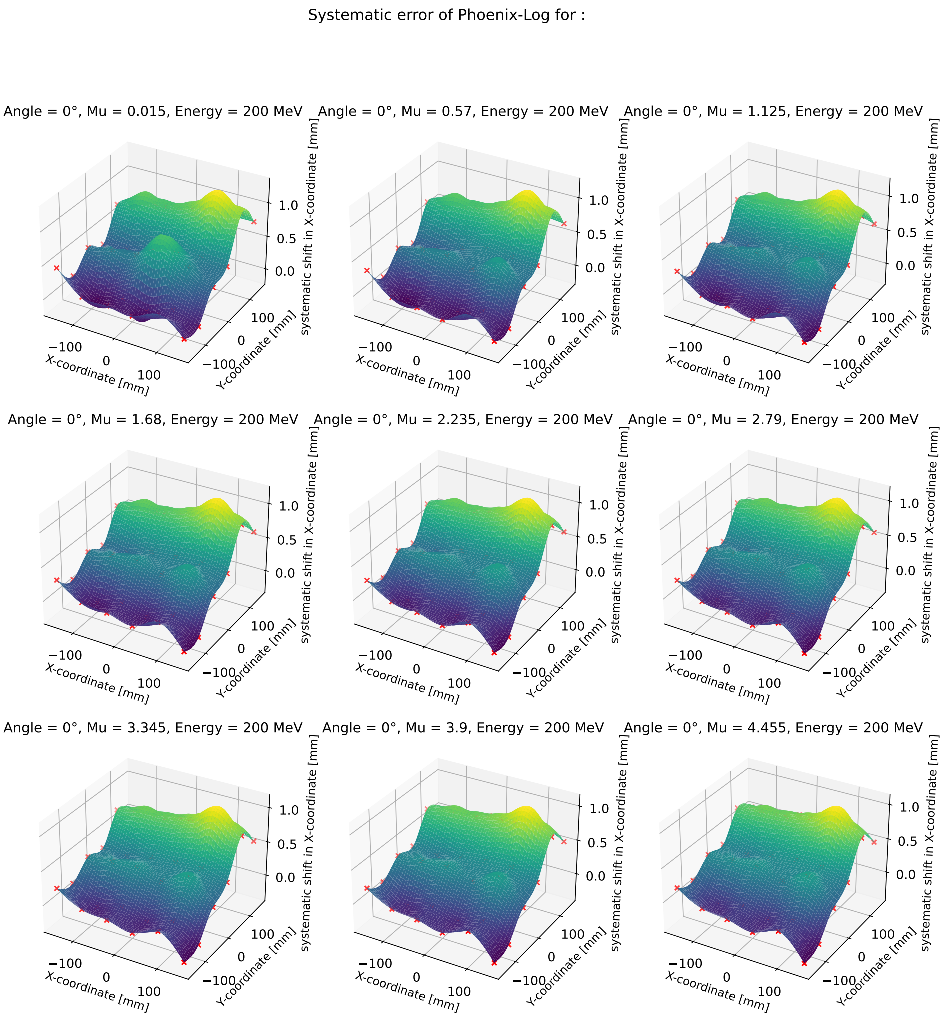

Figure 5.16: Evolution of the systematic error spot by spot in the X coordinate against MUs.

On average, the impact of MU on the accuracy of spot location measurement is minimal. It has been observed that errors caused by MU are consistent throughout the dataset, meaning that each MU has the same error surface. Additionally, there is a slight decrease in the global error as the MU increases. By characterizing MU errors as constants, future measurements can be corrected more effectively, allowing for a focus on other parameters for optimization.

Random error have also been investigated and can reach 0.04mm in X coordinate and -0.075mm in Y coordinate. No pattern have been found.

Energy

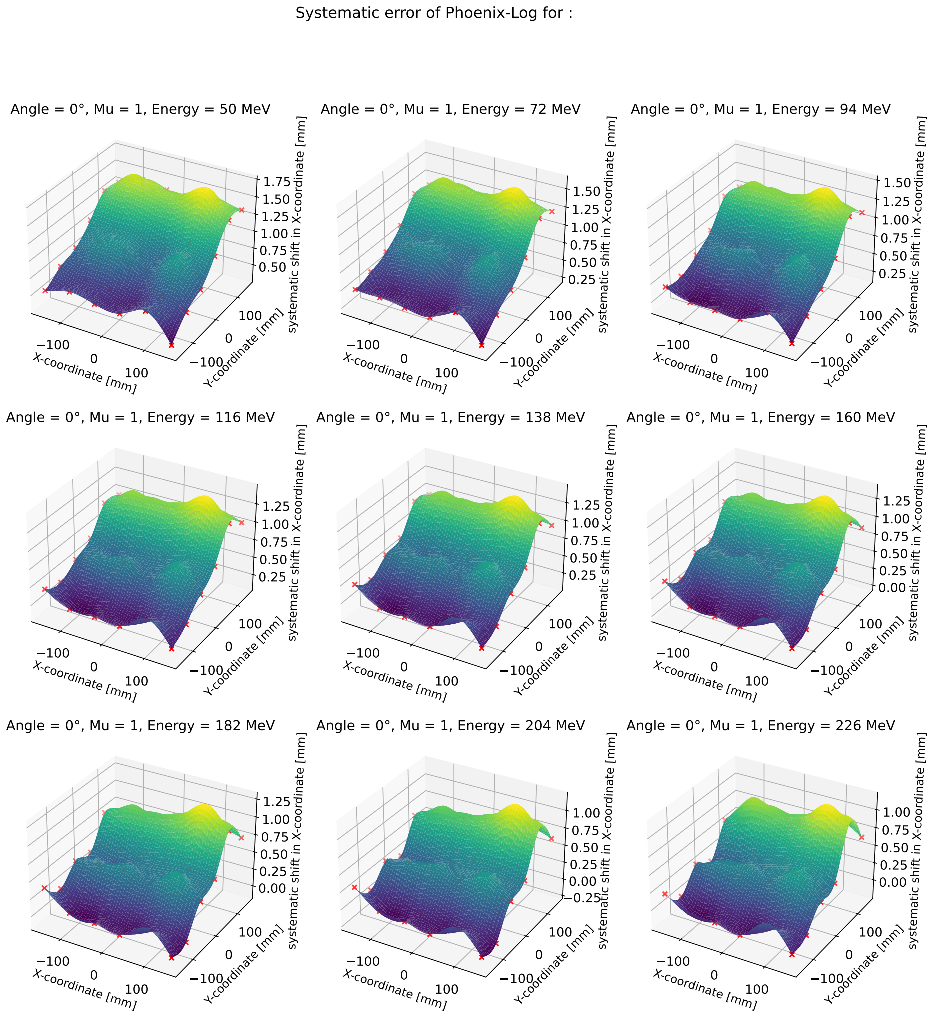

Figure 5.17: Evolution of the systematic error spot by spot in the X coordinate against energies.

Firstly, it is noted that as the energy increases, the overall error decreases. This is consistent with the average error previously analyzed. The error range reduces from 1.5 to 0.5mm for lower energies to 1 to 0mm for higher energies.

However, there is still a strip error localized at (90,90) which affects the accuracy of the measurement. Additionally, the decomposition of the error surfaces in Appendix A and Appendix B reveals that the Plan-Log dataset is bumpy, with errors ranging from 0.5mm to -0.25mm at maximum. There is also a slight tilt, indicating rotation. On the other hand, the Phoenix-Plan dataset is a smooth tilted surface due to the detector rotation for the 0° angle.

As the energy increases, the measurement error becomes more influenced by the Log error, which is evident from the increasing bumpiness of the surface. But there is still a tilt. Therefore, correction of the tilt for the Log and Phoenix datasets will be essential in reducing the error in the measurement.

Random error have also been investigated and can reach -0.04mm in X coordinate and 0.06mm in Y coordinate. No pattern have been found.

Chapter 6

Conclusion and perspectives

In conclusion, this thesis has presented an analysis of the measurement of spot position error using a proton pencil beam scanning delivered by an IBA cyclotron system (ProteusPlus) at UMCG (Groningen) and the Phoenix detector from IBA Dosimetry. The precise determination of spot position error is critical for the effective utilization of Log-Based Patient-Specific Quality Assurance in proton therapy,

This study builds upon Toscano et al.'s previous work on the impact of machine log-file uncertainties on quality assurance, but with a more powerful system and a more accurate detector. The uncertainty related to the information contained in the log files in order to consider them and thus improve PSQA in proton therapy has been investigated. The measurements were performed for a range of energies ([70, 100, 150, 200,226] MeV), angles ([0, 45, 90, 180, 270]°) and MUs ([0.015, 0.1, 0.5, 1, 2, 5]). Through this analysis, several important observations have been made.

Firstly, the gantry angle has an impact on the spot position difference. Each angle induce slight movements of the detector and so require new calculations for correction. Translational corrections were made in both the X and Y directions, as well as rotation correction with (0,0) as the center. However, our measurements have shown that the correction for translation and rotation, though made for each angle, is not perfect, with more work needed to accurately determine the center of rotation.

It was observed that as the energy increased, the overall error decreased. This trend was seen in both the average error and the spot-by-spot measurements without changing the surface's shape. It is also important to note that machine log-files do not store information about the irradiated energy, which is necessary for a full reconstruction of the dose.

Additionally, it has been found that the precision of the spot position is minimally affected by the monitor units (MUs). It is recommended to conduct further specific measurements to analyze the MUs received by the detector while taking into account the correction factor for each gain. In other cases, measurements should focus on other parameters.

Overall, it was observed that the systematic shift is strongly dependent on the spot position and can reach values of 1.09 mm in the X coordinate, and up to -0.57

mm in the Y coordinate. On the other hand, random error are completely negligible against the systematic. Furthermore, the analysis revealed that the Phoenix data produced a smooth surface for the X-coordinate, but a bumpy surface for the Y-coordinate.

Additionally, it was noted that there were strip errors localized at especially at the spot (90,90). Implementing two identical maps, but with one offset, would prevent strip positioning errors and confirm this hypothesis.

An improvement in the data could be achieved by upgrading the holder. Difficulties were encountered during the installation of the detector due to the small alignment markers along the Z axis, making it difficult to place the detector without rotation. Furthermore, in discussion with IBA Dosimetry, and after further analysis, there is a bias in the position of the fiducial in the detector. Accounting for an error of -0.167±0.195mm in X and 0.59±0.205mm in Y direction. By improving the corrections, the accuracy of the measurements could potentially be limited only by the precision of the Log.

In conclusion, this thesis has conducted a comprehensive analysis of spot position error measurements, shedding light on the influence of various parameters on spot errors. Moreover, the study has identified several areas for potential enhancements to further improve the accuracy of these measurements.

The validity of this error model can already be assessed on old treatment plans by comparing the dose volume histogram of the TPS with a MC simulation based on log-corrected. If this comparison shows positive and encouraging results, a live implementation can be made during a real PSQA by incorporating the log data corrected by the model and performing a Monte Carlo calculation.This enables a comparison of the resulting doses with those generated by the TPS and measurements acquired with a detector. If this analysis yields conclusive results, a comprehensive 3D dose comparison can be conducted alongside the TPS.

In the long term, log-based PSQA can be employed retrospectively to verify the treatment. By utilizing the logs in conjunction with Monte Carlo computations, it becomes possible to evaluate the actual dose administered to the patient throughout the entire treatment process.

Appendix A

Plan-Log

A.1 Gantry angle

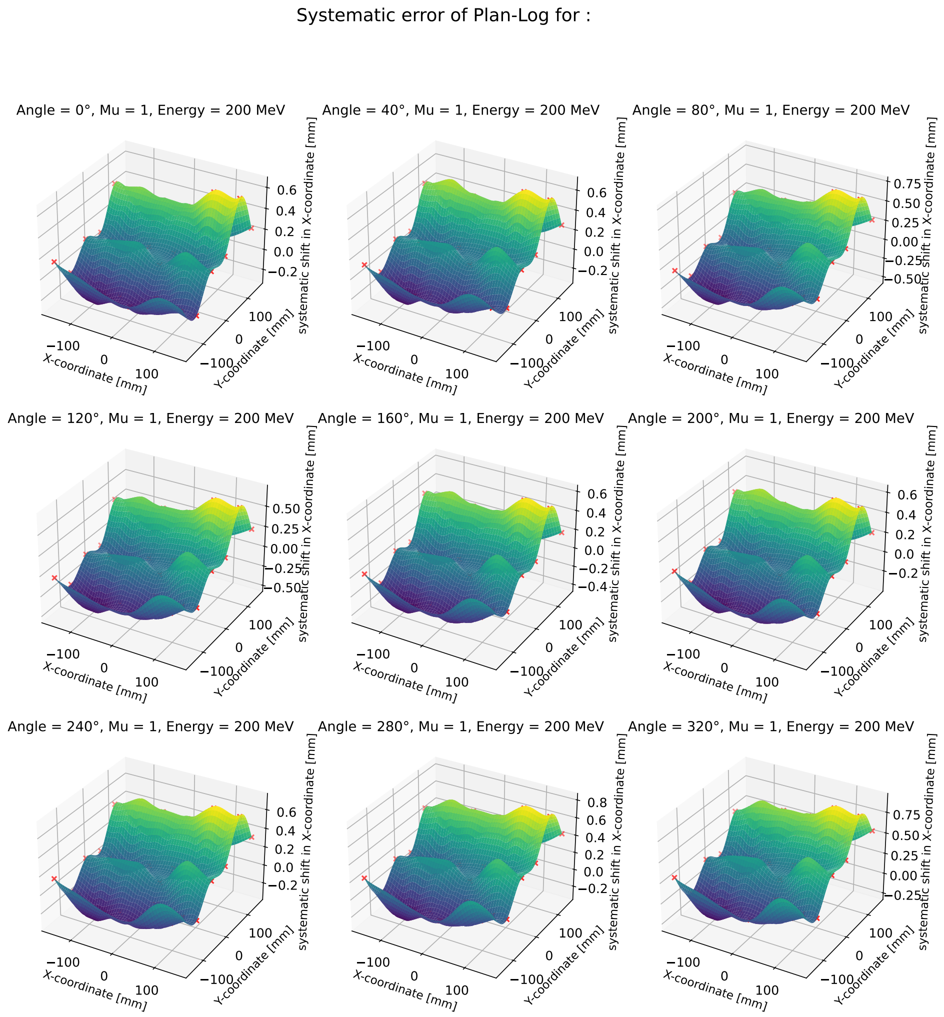
Systematic error of Plan-Log for :

Angle = 0°, Mu = 1, Energy = 200 MeV

Angle = 40°, Mu = 1, Energy = 200 MeV

Angle = 80°, Mu = 1, Energy = 200 MeV

Angle = 120°, Mu = 1, Energy = 200 MeV

Angle = 160°, Mu = 1, Energy = 200 MeV

Angle = 200°, Mu = 1, Energy = 200 MeV

Angle = 240°, Mu = 1, Energy = 200 MeV

Angle = 280°, Mu = 1, Energy = 200 MeV

Angle = 320°, Mu = 1, Energy = 200 MeV

Figure A.1: Evolution of the systematic error spot by spot in the X coordinate against angles.

A.2 MU

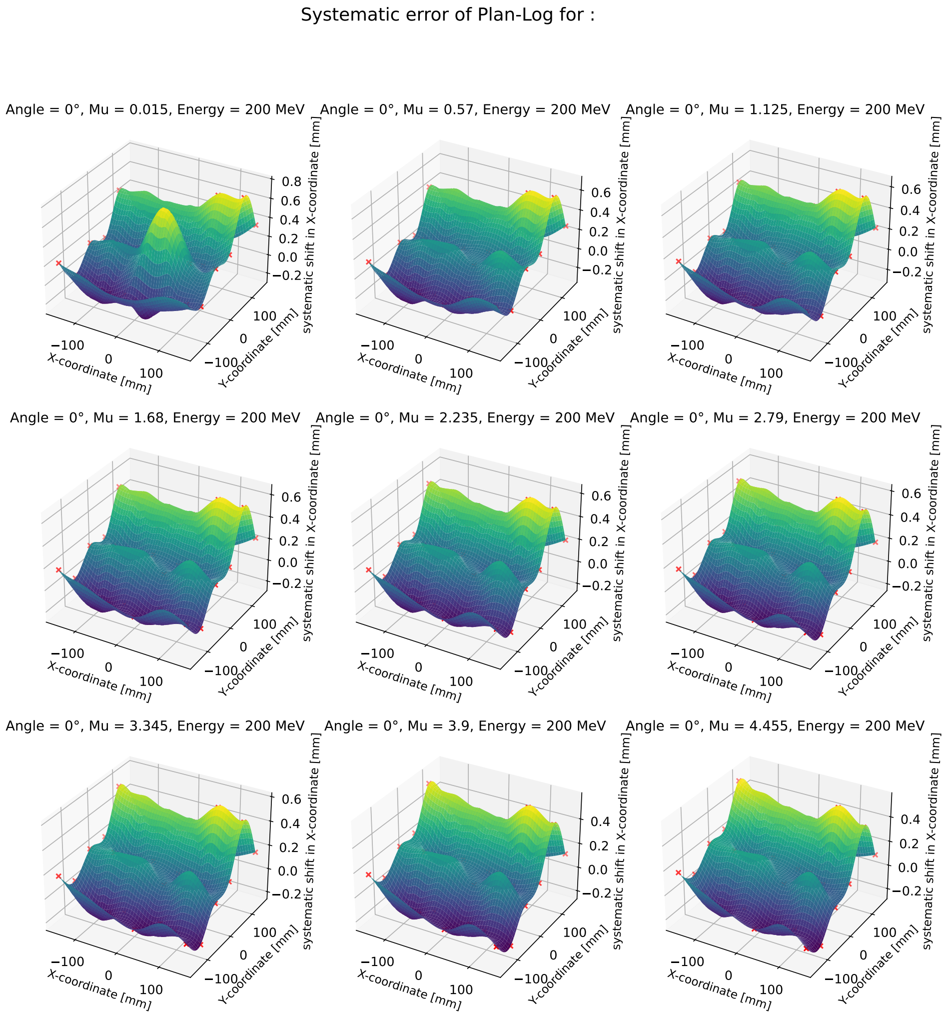

Systematic error of Plan-Log for :

Angle = 0°, Mu = 0.015, Energy = 200 MeV

Angle = 0°, Mu = 0.57, Energy = 200 MeV

Angle = 0°, Mu = 1.125, Energy = 200 MeV

Angle = 0°, Mu = 1.68, Energy = 200 MeV

Angle = 0°, Mu = 2.235, Energy = 200 MeV

Angle = 0°, Mu = 2.79, Energy = 200 MeV

Angle = 0°, Mu = 3.345, Energy = 200 MeV

Angle = 0°, Mu = 3.9, Energy = 200 MeV

Angle = 0°, Mu = 4.455, Energy = 200 MeV

Figure A.2: Evolution of the systematic error spot by spot in the X coordinate against MU.

A.3 Energy

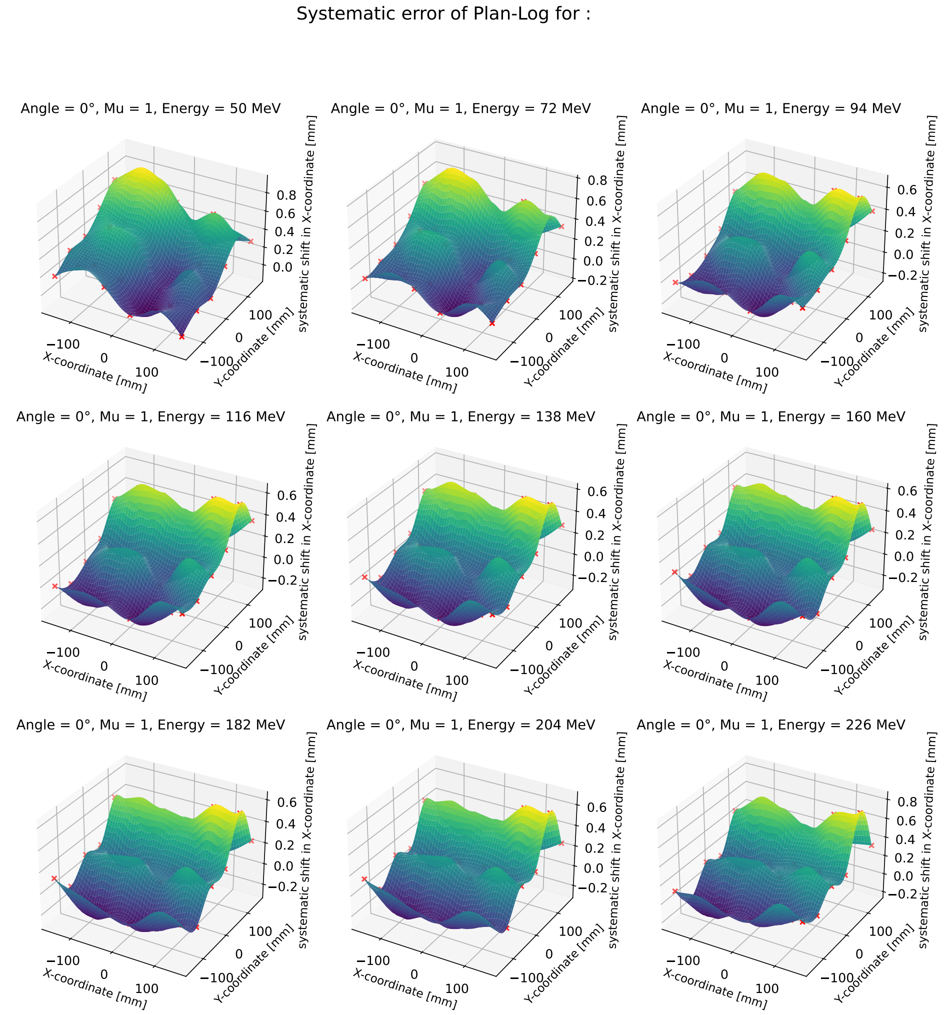

Figure A.3: Evolution of the systematic error spot by spot in the X coordinate against energy.

Appendix B

Phoenix-Plan

B.1 Gantry angle

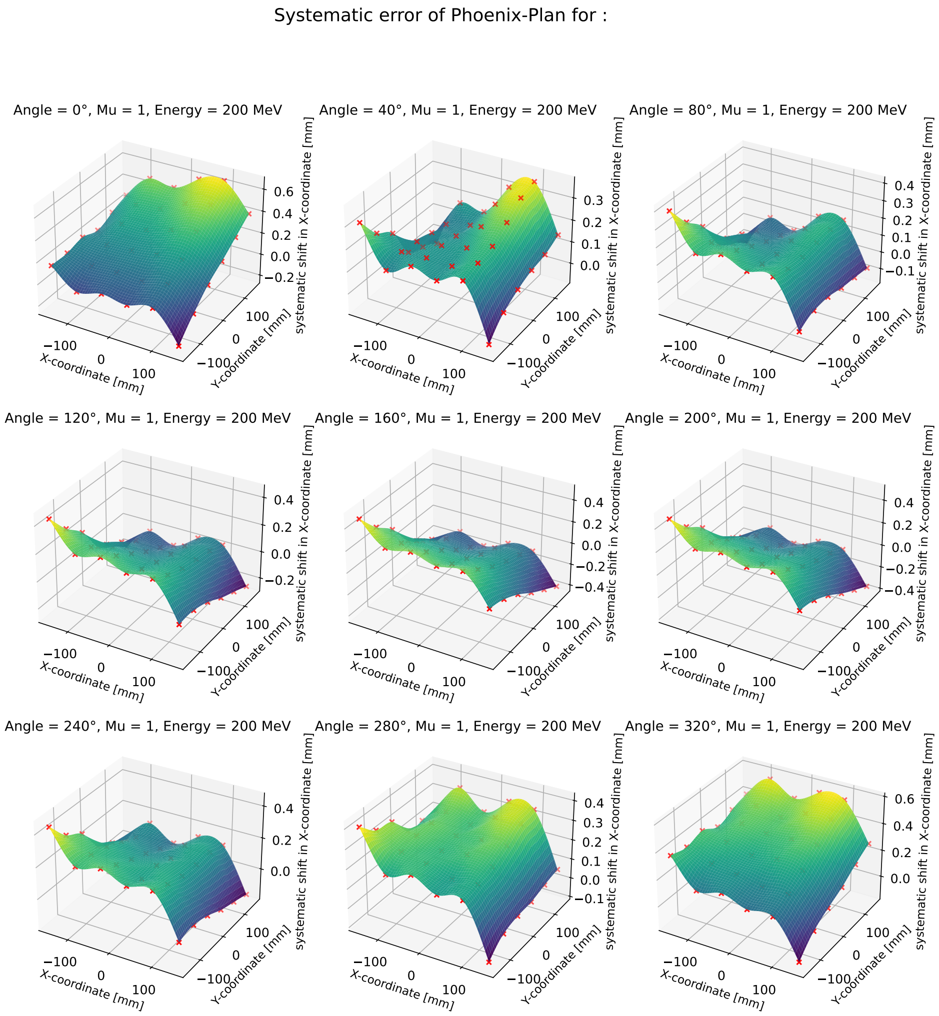

Systematic error of Phoenix-Plan for :

Angle = 0°, Mu = 1, Energy = 200 MeV

Angle = 40°, Mu = 1, Energy = 200 MeV

Angle = 80°, Mu = 1, Energy = 200 MeV

Angle = 120°, Mu = 1, Energy = 200 MeV

Angle = 160°, Mu = 1, Energy = 200 MeV

Angle = 200°, Mu = 1, Energy = 200 MeV

Angle = 240°, Mu = 1, Energy = 200 MeV

Angle = 280°, Mu = 1, Energy = 200 MeV

Angle = 320°, Mu = 1, Energy = 200 MeV

Figure B.1: Evolution of the systematic error spot by spot in the X coordinate against angle.

B.2 MU

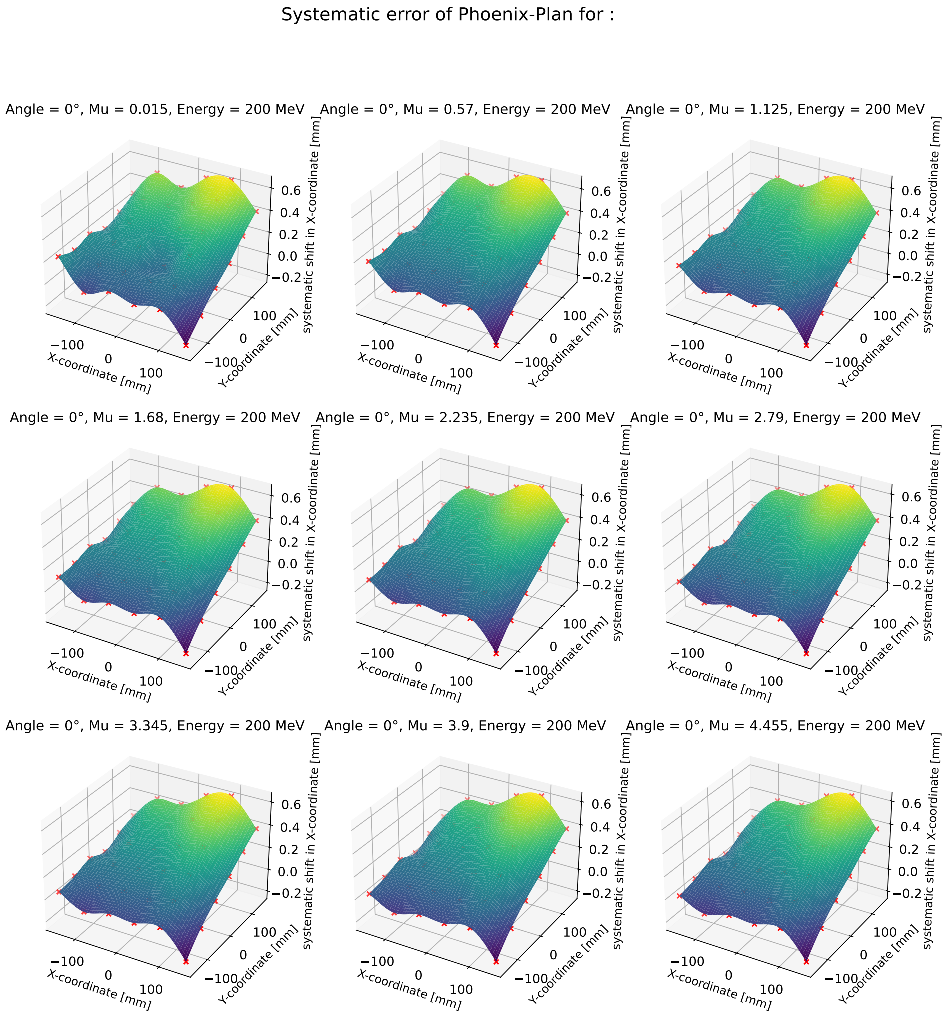

Figure B.2: Evolution of the systematic error spot by spot in the X coordinate against MU.

B.3 Energy

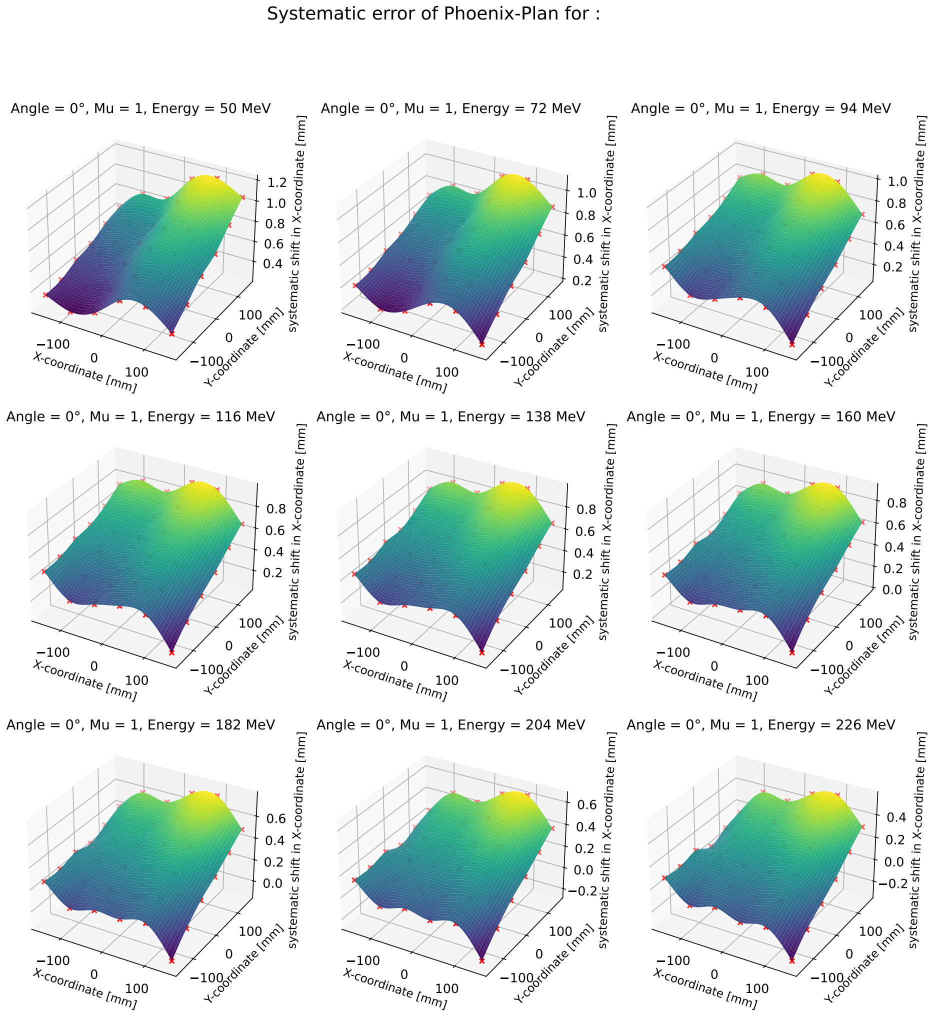

Figure B.3: Evolution of the systematic error spot by spot in the X coordinate against energy.

Bibliography

[1] IBA Dosimetry: MatriXX PT/ONE. URL https://www.iba-dosimetry.com/product/matrixx-one-pt.

[2] IBA Dosimetry: SPHINX COMPACT - The Daily QA Solution. URL https://www.iba-dosimetry.com/product/sphinx-compact/.

[3] Electron beam radiation therapy for skin lymphoma | memorial sloan kettering cancer center. URL https://www.mskcc.org/cancer-care/patient-education/electron-beam-radiation-therapy-skin-lymphoma.

[4] Rad Tech CE, ASRT, ARRT CE, Category A Credits | Radiology Continuing Education. URL https://www.eradimaging.com/course/760.

[5] Linear energy transfer. URL https://en.wikipedia.org/w/index.php?title=Linear_energy_transfer&oldid=1104146875. Page Version ID: 1104146875.

[6] Proteus system - IBA proton therapy. URL http://www.iba-protontherapy.com/proteus.

[7] *Commissioning of Radiotherapy Treatment Planning Systems: Testing for Typical External Beam Treatment Techniques*. Number 1583 in TECDOC Series. INTERNATIONAL ATOMIC ENERGY AGENCY, Vienna, 2008. ISBN 978-92-0-100508-3. URL https://www.iaea.org/publications/7889/commissioning-of-radiotherapy-treatment-planning-systems-testing_for-typical-external-beam-treatment-techniques.

[8] Toutaoui Abdelkader, Amar Aichouche, Kenza Adjidir, and Ahmed Chami. In-air fluence profiles and water depth dose for uncollimated electron beams. *Journal of Medical Physics*, 33, 03 2008. doi: 10.4103/0971-6203.44473.

[9] Bijan Arjomandy, Paige Taylor, Christopher Ainsley, Sairos Safai, Narayan Sahoo, Mark Pankuch, Jonathan B. Farr, Sung Yong Park, Eric Klein, Jacob Flanz, Ellen D. Yorke, David Followill, and Yuki Kase. AAPM task group 224: Comprehensive proton therapy machine quality assurance. *Medical Physics*, 46(8):e678–e705, 2019. ISSN 2473-4209. doi: 10.1002/mp.13622. URL https://onlinelibrary.wiley.com/doi/abs/10.1002/mp.13622. _eprint: https://onlinelibrary.wiley.com/doi/pdf/10.1002/mp.13622.

[10] Maria Francesca Belosi, Antonella Fogliata, Luca Cozzi, Maria Grazia Giri, Cristina Piva, Vittorio Vitolo, and Stefano Tomatis. Pre-treatment patient-specific imrt quality assurance by means of machine learning: A feasibility study. *Physica Medica*, 44:196–202, 2017.

[11] Walt Bogdanich. Radiation offers new cures, and ways to do harm. *New York Times*, 23:A1, 2010.

[12] Pr. Hilde Bosmans. *EPHMD2362 - Technology and Techniques in Radiology*. KULeuven, 2022.

[13] C. Courtois, G. Boissonnat, C. Brusasco, J. Colin, D. Cussol, J. M. Fontbonne, B. Marchand, T. Mertens, S. de Neuter, and J. Peronnel. Characterization and performances of a monitoring ionization chamber dedicated to IBA-universal irradiation head for Pencil Beam Scanning. *Nuclear Instruments and Methods in Physics Research Section A: Accelerators, Spectrometers, Detectors and Associated Equipment*, 736:112–117, 2014. ISSN 0168-9002. doi: https://doi.org/10.1016/j.nima.2013.10.014. URL https://www.sciencedirect.com/science/article/pii/S0168900213013326.

[14] Jacques Ferlay, Isabelle Soerjomataram, Rajesh Dikshit, Sultan Eser, Colin Mathers, Marise Rebelo, Donald Maxwell Parkin, David Forman, and Freddie Bray. Cancer incidence and mortality worldwide: Sources, methods and major patterns in globocan 2012. *International Journal of Cancer*, 136(5):E359–E386, 2015. doi: https://doi.org/10.1002/ijc.29210. URL https://onlinelibrary.wiley.com/doi/abs/10.1002/ijc.29210.

[15] Prof. Bernard Gallez. *WRFAR2100 - Radiochimie, radiotoxicologie et radiopharmacie*. UCLouvain, 2022.

[16] IBA. *myQA Phoenix User's Guide*. Ion Beam Application, 2022.

[17] J. E. Johnson, C. Beltran, H. Wan Chan Tseung, D. W. Mundy, J. J. Kruse, T. J. Whitaker, M. G. Herman, and K. M. Furutani. Highly efficient and sensitive patient-specific quality assurance for spot-scanned proton therapy. *PLOS ONE*, 14(2):1–16, February 2019. doi: 10.1371/journal.pone.0212412. URL https://doi.org/10.1371/journal.pone.0212412. Publisher: Public Library of Science.

[18] Eric E Klein, Joseph Hanley, John Bayouth, Fang-Fang Yin, William Simon, Sean Dresser, Christopher Serago, Francisco Aguirre, Lijun Ma, Bijan Arjomandy, et al. Task group 142 report: Quality assurance of medical accelerators a. *Medical physics*, 36(9Part1):4197–4212, 2009.

[19] Gabriel Meier, Tim Brandt, Ndeserua Chofor, Sebastian Gerum, Martin Hoheisel, Harald Paganetti, Damien C Weber, and Anthony J Lomax. An automated monte carlo log-file-based pre-treatment quality assurance tool for scanned proton beams. *Radiation Oncology*, 10(1):1–11, 2015.

[20] Radhe Mohan. A review of proton therapy – current status and future directions. *Precision Radiation Oncology*, 6(2):164–176, 2022. doi: https://doi.org/10.1002/pro6.1149. URL https://onlinelibrary.wiley.com/doi/abs/10.1002/pro6.1149.

[21] Wayne D Newhauser and Rui Zhang. The physics of proton therapy. *Physics in Medicine & Biology*, 60(8):R155, mar 2015. doi: 10.1088/0031-9155/60/8/R155. URL https://dx.doi.org/10.1088/0031-9155/60/8/R155.

[22] Pr. Johan Nuyts, Prof. Dr. K. Goffin, and Prof. Dr. Kristof Baete. *[G0Z64a] - Technology and Techniques in Nuclear Medicine.* KULeuven, 2022.

[23] Anupam Saini, Manish Kumar, Shailendra Bhatt, Vipin Saini, and Anuj Malik. Cancer causes and treatments. 07 2020.

[24] Domenico Scandurra, Sara Morlino, Alfredo Mirandola, Giulia Russo, Vittoria D'Avino, Antonina Monaco, Vittoria Bruzzaniti, Giuseppe A P Cirrone, Giacomo Cuttone, and Roberto Guglielmi. Integration of a monte carlo algorithm for prompt-gamma evaluation in a log-file-based qa system for proton therapy. *Physics in Medicine & Biology*, 61(2):763, 2016.

[25] Pr. Edmond Sterpin. *WRDTH3120 - Dosimétrie en radiothérapie et contrôle de qualité.* Imagerie Médicale, Radiothérapie et Oncologie (MIRO), 2021.

[26] Pr. Edmond Sterpin. *WRDTH3160 - Technology, Dosimetry and Treatment Planning in Radiotherapy.* Imagerie Médicale, Radiothérapie et Oncologie (MIRO), 2022.

[27] S Toscano, K Souris, C Gomà, A Barragán-Montero, S Puydupin, F Vander Stappen, G Janssens, A Matic, X Geets, and E Sterpin. Impact of machine log-files uncertainties on the quality assurance of proton pencil beam scanning treatment delivery. *Physics in Medicine & Biology*, 64(9):095021, apr 2019. doi: 10.1088/1361-6560/ab120c. URL `https://dx.doi.org/10.1088/1361-6560/ab120c`.

[28] X. R. Zhu, F. Poenisch, M. Lii, G. O. Sawakuchi, U. Titt, M. Bues, X. Song, X. Zhang, Y. Li, G. Ciangaru, H. Li, M. B. Taylor, K. Suzuki, R. Mohan, M. T. Gillin, and N. Sahoo. Commissioning dose computation models for spot scanning proton beams in water for a commercially available treatment planning system. *Medical Physics*, 40(4):041723, 2013. doi: https://doi.org/10.1118/1.4798229. URL `https://aapm.onlinelibrary.wiley.com/doi/abs/10.1118/1.4798229`.

[29] Xiaorong Zhu, Yupeng Li, Dennis Mackin, Heng Li, Falk Poenisch, Andrew Lee, Anita Mahajan, Steven Frank, Michael Gillin, Narayan Sahoo, and Xiaodong Zhang. Towards effective and efficient patient-specific quality assurance for spot scanning proton therapy. *Cancers*, 7:631–647, 06 2015. doi: 10.3390/cancers7020631.

UNIVERSITE CATHOLIQUE DE LOUVAIN

Faculté des sciences

Place des sciences, 2 bte L6.06.01, 1348 Louvain-la-Neuve, Belgique | **www.uclouvain.be/sc**